Modelling the aeroelastic response and flight dynamics of a hingeless rotor helicopter including the effects of rotor-fuselage aerodynamic interaction

I. Goulos
i.goulos@cranfield.ac.uk
School of Aerospace
Transport and Manufacturing
Cranfield University
Bedford
UK

ABSTRACT

This paper presents a mathematical approach for the simulation of rotor-fuselage aerodynamic interaction in helicopter aeroelasticity and flight dynamics applications. A Lagrangian method is utilised for the numerical analysis of rotating blades with nonuniform structural properties. A matrix/vector-based formulation is developed for the treatment of elastic blade kinematics in the time-domain. The combined method is coupled with a finite-state induced flow model, an unsteady blade element aerodynamics model, and a dynamic wake distortion model. A three-dimensional, steady-state, potential flow, source-panel method is employed for the prediction of induced flow perturbations in the vicinity of the fuselage due to its presence in the free-stream and within the rotor wake. The combined rotor-fuselage model is implemented in a nonlinear flight dynamics simulation code. The integrated approach is deployed to investigate the effects of rotor-fuselage aerodynamic interaction on trim performance, stability and control derivatives, oscillatory structural blade loads, and nonlinear control response for a hingeless rotor helicopter modelled after the Eurocopter Bo105. Good agreement is shown between flow-field predictions and experimental measurements for a scaled-down isolated fuselage model. The proposed numerical approach is shown to be suitable for real-time flight dynamics applications with simultaneous prediction of structural blade loads, including the effects of rotor-fuselage aerodynamic interaction.

Paper No. 4153. Manuscript received 16 February 2014, revised version received 27 July 2014, accepted 22 September 2014.

https://doi.org/10.1017/S0001924000010563 Published online by Cambridge University Press

NOMENCLATURE

B_j	influence coefficient of the jth source panel element on the evaluation point with co-ordinates (x, y, z) m
C, **D**	wake curvature influence matrix (Krothapalli and Zhao models, respectively)
g	gravitational constant, m/sec^2
I_{xx}, I_{yy}, I_{zz}, I_{xz}	Fuselage roll, pitch, yaw, and roll-yaw moments of inertia, kg · m^2
K_{Re}	wake curvature parameter
$\mathbf{L}^c$, $\mathbf{L}^s$	Cosine and sine inflow gain matrices
$\mathbf{M}^c$, $\mathbf{M}^s$	Cosine and sine apparent mass matrices
n	unit vector perpendicular to dS of S_b positive towards the direction of the potential jump, m
N_b, N_p	number of blades and quadrilateral panel elements
p, q, r	angular velocity components of the fuselage expressed about the fuselage reference axes frame, rad/sec
P_{rotor}	main rotor power required, kW
$\bar{P}_n^m(\nu)$	normalised associated Legendre function of first kind
$P(x, y, z)$	induced potential evaluation point with Cartesian co-ordinates (x, y, z)
$\bar{q}, \bar{p}$	normalised pitch and roll rates = $\frac{q}{\Omega}$, $\frac{p}{\Omega}$
r	geometric distance of source panel from evaluation point $P(x, y, z)$, m
r, R	local and total rotor blade radius, m
$\bar{r}$	non-dimensional radial co-ordinate on the rotor disk = $\frac{r}{R}$
S	state of wake spacing, = $2\pi V_T$
S_b	three-dimensional body surface, m^2
t	time, sec
$\bar{t}$	non-dimensional time = Ωt
V, V_T	flow parameter and total flow at the rotor disk plane, dimensionless
V_{flight}	helicopter flight speed, m/sec
$\bar{u}$, $\bar{v}$, $\bar{w}$	normalised fuselage induced velocity perturbations
v	induced velocity perturbation vector = $[u\ v\ w]^T$, ms^{-1}
$\mathbf{V}^c$, $\mathbf{V}^s$	Cosine and sine mass flow parameter matrices
$\mathbf{V}_\infty$	free-stream velocity vector, = $[U_\infty\ V_\infty\ W_\infty]^T$, ms^{-1}
u, v, w	translational velocity components of the fuselage expressed about the fuselage reference axes frame, m/sec
X	function of wake skew angle, = Tan $\lvert\chi/2\rvert$
X, Y, Z, L, M, N	external forces and moments applied about the aircraft CG, N, Nm

Greek symbols

α_f , α_s	fuselage and rotor shaft incidences, deg
α_j^r, β_j^r	non-dimensional wake induced flow expansion coefficients
$\bar{\mu}$	advance ratio, $\frac{V_{flight}}{\Omega R}$
β_0, β_{1c}, β_{1s}	rotor coning, longitudinal, and lateral rotor flapping angles, rad

https://doi.org/10.1017/S0001924000010563 Published online by Cambridge University Press

χ	wake skew angle, $= \pi/2 - \text{Arctan}\left\|\frac{\lambda_f + \lambda_m}{\bar{\mu}}\right\|$ rad
κ_c, κ_s	longitudinal and lateral wake curvature values
$\lambda(\bar{r}, \psi, \bar{t})$	non-dimensional wake-induced velocity at the rotor disk
λ_f	normalised free-stream velocity normal to the rotor disk, $= \frac{V_n}{\Omega R}$
λ_m	normalised mean wake-induced velocity normal to the rotor disk, $= \sqrt{3}\alpha_1^0$
μ, σ	doublet and source strength per unit area, 1/sec, m/sec
Ω	shaft rotor speed, rad/sec
Φ_∞, Φ_i	free-stream and induced velocity potential, m^2/sec
Φ_{total}	total velocity potential = $\Phi_\infty + \Phi_i$, m^2/sec
Φ_{total}^{int}	total internal potential, enclosed by S_b, m^2/sec,
ψ	azimuthal co-ordinate on the rotor disk, rad
$\psi(t)$	azimuth angle of the ith blade, $i = 1, \ldots N_b$, rad
τ_n^{mc}, τ_n^{ms}	cosine and sine generalised aerodynamic pressure coefficients
τ_x, τ_s, τ_r	time-constants of dynamic wake skew, vortex spacing, and wake curvature
Θ, Φ, Ψ	fuselage pitch, roll, and yaw attitude angles, rad
$\theta_0, \theta_{1s}, \theta_{1c}$	collective, longitudinal cyclic, and lateral cyclic pitch control angles, rad
$\zeta_0, \zeta_{1s}, \zeta_{1c}$	average, and first harmonic rotor lead-lag angles, rad
$\dot{(\,)}, \ddot{(\,)}, (\,)', (\,)''$	first and second derivatives with respect to time t and blade radius r
$\bar{(\,)}^{r,n}$	harmonic number indices
$\bar{(\,)}$	signifying quantity normalisation, $= \frac{()}{R}$ for radial distances, $\frac{()}{\Omega}$ for angular rates, $(\,)\cdot\Omega$ for time, $\frac{()}{\Omega \cdot R}$ for velocities
$(\,)_{body}$	referring to the region enclosed by the body surface S_b
$(\,)_{i,f}$	blade or panel indices
$(\,)_{j,n}$	Legendre function polynomial number indices
$(\,)_{qs}$	referring to a quasi-steady state condition

1.0 INTRODUCTION

1.1 Background

The main rotor of a helicopter acts as a lifting, propulsive, and control device simultaneously. Thus, flight dynamics simulation must not only produce accurate predictions of rotor power and thrust, but it must also provide precise estimates of the time-dependent rotor forces and moments exerted on the aircraft fuselage. Especially regarding cases where higher-frequency harmonic content is desirable in the analysis, it is essential that the aeroelastic response of the rotor blades is accurately predicted. This not only requires sophisticated models for structural and rotor dynamics but it also entails the employment of equally advanced rotor inflow and blade element aerodynamics models. The aeroelastic response of the main rotor is highly dependent on the encountered flow-field conditions. Hence, in the context of helicopter flight dynamics, accurate simulation of aeroelasticity requires that the nature of the surrounding complex flow-field is adequately captured.

In order to understand the complex flow-field within which the main rotor operates, it is essential that the individual contributing components affecting the surrounding flow are identified

https://doi.org/10.1017/S0001924000010563 Published online by Cambridge University Press

and modelled at an acceptable level of detail. The complexity of the approach may depend on application requirements and is usually limited predominantly by the associated computational cost. Investigations focusing on the underlying physics of the three-dimensional rotor inflow may require a rather sophisticated modelling approach. This may possibly include the employment of free-wake vortex filament methods[1], vorticity transport simulation[2], or maybe even a viscous computational fluid dynamics (CFD) analysis[3]. The associated computational cost may then be considered acceptable for the designated application. However, a more computationally efficient modelling approach may be desired with respect to real-time flight dynamics applications.

Although the rotor wake is the dominant contributing factor to the encountered flow-field conditions, the aircraft fuselage may also serve to alter the flow pattern in the vicinity of the rotor tip-path plane. Current design trends dictate for helicopters to be increasingly more compact in order to raise attainable airspeed and consequently reduce operational costs[4]. This trend essentially leads to the main rotor being closer to the fuselage surface, thus increasing the effective aerodynamic interaction between the two components. This increasingly strong aerodynamic interaction may also serve to modify the flight dynamics of the aircraft. Therefore, in the context of nonlinear flight dynamics simulation of conceptual rotorcraft, it is essential that the dominant rotor-fuselage aerodynamic interaction effects are accounted for and modelled at an acceptable level of fidelity.

1.2 Helicopter rotor-fuselage aerodynamic interaction

During flight, the presence of the fuselage in the vicinity of the main rotor affects the surrounding flow-field in two different manners[5]; (1) the induced velocity perturbation that appear solely due to the presence of the fuselage in the free-stream and, (2) the velocity perturbations due to the effective distortion of the wake when it impinges on the aircraft fuselage. The former effect is relatively simple to model and can be captured using potential flow theory. However, the latter component is considerably more complex in nature. Therefore, sophisticated modelling of the three-dimensional rotor wake is essential in order to capture it properly[3].

Several studies are reported in the literature where the effects of fuselage induced flow on rotor performance and loads have been investigated experimentally and analytically. Crimi and Trenka[6] developed a methodology based on potential flow theory for the simultaneous modelling of rotor wake and fuselage aerodynamics. Their goal was to predict the combined downwash at the rotor tip-path plane. Keys[7] deployed a source-panel method in order to investigate the effects of fuselage induced velocity perturbations on the rotor blade angle-of-attack in forward flight conditions. Johnson and Yamauchi[8] attempted to examine the general effects due to the aerodynamic interference between the main rotor and the fuselage, using a generic-axisymmetric fuselage geometry.

The literature contains a substantial amount of references where the flow around an isolated helicopter fuselage has been studied independently of the main rotor inflow. Berry and Althoff[5] followed a numerical and experimental approach in order to investigate the properties of the flow-field in the vicinity of the experimental ROBIN (ROtor Body INteractions) fuselage[9]. Their approach was based on the development of a potential flow source-panel method which was used in order to predict the steady-state induced velocity perturbations around the isolated fuselage. Perturbation velocities were computed and compared with experimental measurements made with a laser velocimeter at the rotor tip-path plane (rotor removed). Their numerical approach was found to agree well with the measured data, apart from the vicinity close to the rotor hub where large amounts of separated flow were observed.

Ghee *et al*[10] followed an experimental approach in order to investigate the rotor wake geometry and quantify the induced flow in the vicinity of a scaled-down model of a helicopter rotor in forward flight. Extensive flow-field measurements were also conducted around the ROBIN fuselage[9]. Berry

https://doi.org/10.1017/S0001924000010563 Published online by Cambridge University Press

and Bettschart[4] described a comprehensive approach for the nonlinear modelling of rotor-fuselage aerodynamic interaction effects. A comparative evaluation was carried out between three nonlinear analytical methods and experimental data regarding the flow-field in the vicinity of the Dauphine helicopter. Good agreement was observed between nonlinear predictions and experimental data, considering the steady-state properties of the flow-field. However, the unsteady features of the flow were not captured adequately by any of the employed numerical methods.

Lorber and Egolf[11] described a computational method targeting the treatment of the aerodynamic interaction between the main rotor and the fuselage. Their numerical approach included the use of a modified lifting line/prescribed wake induced flow analysis coupled with a source-panel fuselage model. The authors of Ref. 11 were not able to validate the primary outcome of their analysis, which was the estimation of vibratory loads induced by the main rotor on the fuselage, due to lack of experimental data. Renaud *et al*[3] compared the accuracy of three different viscous flow solvers (CFD) in terms of predicting the flow-field in the vicinity of an isolated fuselage, as well as for the coupled rotor-fuselage system of the Dauphin 365N helicopter. Lee *et al*[12] developed a three-dimensional inviscid flow solver based on an unstructured mesh. Their tool was subsequently deployed for the evaluation of the unsteady flow-field in the vicinity of the UH-60 helicopter using the ROBIN fuselage geometry.

Kelly *et al*[13] employed Brown's Vorticity Transport Model[2] in order to investigate the rotor blade loading, the resultant wake geometry, and the acoustic noise radiation for the HART II experimental rotor system[14]. Simulations were carried for the integrated rotor-fuselage configuration as well as for the isolated rotor. The authors of Ref. 13 noted that inclusion of aerodynamic interference between the main rotor and the fuselage yields a marked improvement in the prediction of the vortex positions when compared to simulations performed for the isolated rotor.

O'Brien[15] and O'Brien and Smith[16,17] investigated the effects of rotor-fuselage aerodynamic interaction using CFD methods employing lower-order modelling fidelity. Their numerical approach essentially modelled the rotor as an actuator disk. The unsteady circulation produced by the rotor blades was modelled by inserting discrete source terms in the computational grid, whose magnitude was determined from momentum or blade element theory. This approach was found to be reasonably accurate for the prediction of both steady and unsteady aerodynamic fuselage loads.

Biedron and Lee-Rausch[18] described an unsteady, Reynolds-averaged, Navier-Stokes CFD solver for unstructured grids, that was employed in order to compute rotor airloads for the UH-60A helicopter at high-speed and high thrust conditions, respectively. The nonlinear CFD method was numerically coupled with the computational structural dynamics (CSD) model of the comprehensive rotorcraft code CAMRAD II[19] in order to obtain rotor trim, as well as estimate the dynamic response of the elastic blades to external forcing. Simulations were carried out both with and without accounting for the influence of the fuselage. Biedron and Lee-Rausch noted that the effect of the fuselage on rotor airloads was more notable in the radially inboard sections of the blade ($r/R \leq 0{\cdot}5$), when compared to the radially outboard stations. It was also observed that the mean airloads at the outboard blade sections were virtually unchanged by the presence of the fuselage whilst only minimal differences were noted for the inboard stations. Inclusion of the fuselage at high-speed conditions resulted in generally improved airloads predictions, predominantly considering the forward part of the rotor disk. Inclusion of the fuselage at high thrust conditions did not consistently improve the correlations with measured data and the mean airloads were virtually unchanged.

Other notable work where the aerodynamic influence of the fuselage has been included in nonlinear predictions of airloads, aeroelastic blade deformations, and rotor trim using a coupled CFD/CSD approach, includes that of Boyd[20], Sa *et al*[21], Smith *et al*[22], and Van der Wall *et al*[23].

https://doi.org/10.1017/S0001924000010563 Published online by Cambridge University Press

1.3 Scope of present work

The aerodynamic influence of the fuselage has been routinely modelled in non-real-time coupled CFD/CSD formulations but has not been catered for in real-time flight dynamics applications. This is due to the large computational overhead associated with high-complexity modelling methods employed in coupled CFD/CSD methodologies, such as vorticity transport modelling, Reynolds-averaged or time-accurate Navier-Stokes solvers, and free-vortex wake filament methods. This essentially prohibits the deployment of such formulations in real-time flight dynamics applications such as nonlinear control response analysis. As a result, the associated rotor-fuselage interaction effects on the aeroelastic rotor response and consequently on the flight dynamics of the aircraft in terms of trim, stability, and control, have not been adequately covered in the literature. Furthermore, the viability of modelling rotor-fuselage interaction effects in a real-time flight dynamics simulation environment through a standardised numerical approach, has not been addressed nor documented.

In light of the existing literature, the general scope of this work is to develop an integrated approach for the treatment of rotor-fuselage aerodynamic interaction effects in real-time helicopter flight dynamics applications. The specific objectives of this paper can be outlined as follows:

1. To describe a comprehensive mathematical model for real-time flight dynamics simulation that also employs sufficient modelling fidelity for prediction of aeroelastic rotor blade loads.
2. To demonstrate the feasibility of modelling the effects of rotor-fuselage aerodynamic interaction in real-time flight dynamics simulation using a standard numerical approach based on potential flow.
3. To perform a first-order identification of the effects of rotor-fuselage aerodynamic interaction on the predicted flight dynamics and oscillatory blade loads for a hingeless rotor helicopter.
4. To evaluate the computational requirements associated with the execution of the proposed approach and assess its suitability for real-time flight dynamics applications.

The mathematical model presented in this paper for the simulation of rotor-fuselage aerodynamic interaction is broadly arranged as follows; Initially, a Lagrangian approach is deployed in order to estimate the natural vibration characteristics of rotating blades with nonuniform structural properties. A numerical formulation is utilised for the treatment of rotor blade flexibility in real-time flight dynamics applications, whilst employing sufficient modelling fidelity for simultaneous prediction of oscillatory blade loads. The combined approach is coupled with a finite-state induced flow model, an unsteady blade element aerodynamics model, and a dynamic wake distortion model.

A three-dimensional, steady-state, potential flow source-panel method is developed. The scheme is based on the principle of constant internal potential and is capable of estimating the flow-field anywhere within the three-dimensional domain. The panel method is deployed in order to predict the induced velocity perturbations in the vicinity of the fuselage due to its presence in the free-stream and within the rotor wake. The source-panel approach is coupled with the developed aeroelastic rotor model by superimposing the fuselage induced velocity perturbations on the overall inflow at the rotor tip-path plane. The aeroelastic rotor response and the fuselage induced flow are solved simultaneously due to their implicit coupling through the rotor wake. The combined aeroelastic rotor-fuselage model is implemented in a nonlinear flight dynamics simulation code. The dynamic (rigid-body) fuselage equations found in the literature[24] that are implicitly coupled in the roll-yaw degrees of freedom (DOFs), are manipulated mathematically in order to derive a set of fully explicit, first-order ordinary differential equations (ODEs) that can be evaluated explicitly.

Results are presented in terms of three-dimensional induced velocity perturbations at the main

https://doi.org/10.1017/S0001924000010563 Published online by Cambridge University Press

rotor tip-path plane for a scaled-down isolated fuselage model[9]. A comparative evaluation is carried out between numerical results and flow-field measurements conducted at the NASA Langley subsonic wind tunnel[5]. Good agreement is shown between potential flow prediction and measured data with the exception of the vicinity close to the rotor hub. The integrated approach is subsequently deployed in order to investigate the effects of rotor-fuselage aerodynamic interaction on: trim performance, stability and control (S & C) derivatives, oscillatory blade loads, and nonlinear control response for a hingeless rotor helicopter modelled after the Eurocopter Bo105. Comparisons are carried out with flight test measurements, system identification results, and nonlinear predictions made with a non-real-time, high-complexity flight dynamics simulation code[25].

2.0 THEORETICAL MODEL DEVELOPMENT

The modelling approach employed for the analysis presented in this paper, effectively accounts for the dominant physical phenomena that influence the aeroelastic response of a hingeless rotor and consequently the flight dynamics of the aircraft. These effects are related to a wide-range of engineering disciplines which include; fuselage aerodynamics, structural and rotor dynamics, inflow dynamics, unsteady nonlinear aerodynamics, and dynamic wake distortion. This section elaborates on the core engineering principles that have been utilised in order to formulate a robust numerical approach for modelling rotor-fuselage interaction effects in real-time flight dynamics applications.

The proposed approach can be regarded as a combination of a steady-state potential flow method coupled with an unsteady, nonlinear, aeroelastic rotor model. The aerodynamic coupling is based on the assumption that the steady-state components of the fuselage induced velocity perturbations can be superimposed on the unsteady rotor inflow. The effect of wake distortion due to its impingement on the fuselage body is neglected. However, the effect of modifying the vorticity in the trailing rotor wake due to any change in the aerodynamic response of the blades, is thoroughly accounted for.

2.1 Structural dynamics: Natural vibration characteristics of helicopter rotor blades

A minimum potential energy approach based on Lagrange's equation of motion is utilised in order to obtain the natural vibration characteristics of the rotor blades for flap, lag, and torsion[26]. The blade is treated as a continuous system of nonuniform structural properties. A finite series of assumed deformation functions based on Bernoulli-Euler and classical torsional vibration theory, is employed for the approximation of the time variations of the blade's strain and kinetic energy for each DOF. Integral expressions describing the generalised centrifugal loads exerted on the blade are incorporated. Inserting the expressions for strain, kinetic energy, and generalised centrifugal loads into Lagrange's equation of motion, results in the mathematical formulation of the eigenproblem which is solved with customary matrix techniques. The solution of the eigenproblem along with the use of a proper normalisation condition, essentially leads to the flap-lag-torsion natural frequencies and mode shapes for the nonuniform rotating blade.

Neither inertial nor elastic coupling between flap, lag, and torsion is taken into account during the formulation of the Lagrangian eigenproblem. Therefore, all degrees of freedom are treated separately in the modal analysis. This is due to the fact that the Lagrangian method is designated for dynamic response analysis in the time-domain, where the nonlinear aerodynamic and inertial loads can be treated as a time-history of external forcing. Although elastically uncoupled flap-lag-torsion

https://doi.org/10.1017/S0001924000010563 Published online by Cambridge University Press

blade motion is considered in this paper, the modal characteristics of any employed theory can be used with any level of coupling. It is noted that that the numerical approach presented in this paper maintains the inertial coupling between the flap-lag-torsion through proper inclusion of the inertial blade loads in the derived equations of elastic blade motion. The Lagrangian method has been extensively described and validated in Refs 26 and 27.

2.2 Rotor dynamics: Simulation of flexible rotor blade dynamics

The described Lagrangian approach has been coupled with the nonlinear aeroelastic rotor model presented in Refs 28-30. The aforementioned model has been previously developed by the author for the simulation of rotor blade flexibility in real-time flight dynamics applications, whilst employing sufficient modelling fidelity for simultaneous prediction of oscillatory blade loads. The overall method has been formulated using linear algebraic expressions and accounts for the inclusion of all nonlinear inertial terms associated with large blade deflections and fuselage angular motions.

In order to accomplish robustness and establish applicability in real-time, a novel, second-order accurate, finite-difference algorithm, originally developed for time-accurate free-wake analysis[31], is employed for the temporal discretisation of elastic blade motion in the time-domain. The employed methodology results in readily available integral expressions that provide the aeroelastic rotor loads, expressed directly in the standard flight dynamics fuselage axes reference system (Fig. 19(a)).

The author's mathematical model has been validated extensively in Refs 28-30 and 32 through comparison with experimental data derived from flight tests and wind-tunnel measurements. Validation has been carried out in terms of flight dynamics, oscillatory blade loads, and rotor induced vibration for the hingeless rotor of the Bo105[28-30] and the articulated rotor of the Aerospatiale SA 330 helicopter[29,32]. Appendix A contains a comprehensive mathematical description of the employed modelling approach, thus further elaboration within this section shall be omitted.

2.3 Fuselage aerodynamics: Potential flow induced velocity perturbations

Consider a three-dimensional body with solid boundaries defined by a surface S_b, immersed within a control volume with free-stream conditions $\mathbf{V}_\infty = [U_\infty \; V_\infty \; W_\infty]^T$. The governing equation for the velocity potential of an inviscid, incompressible, and irrotational flow is given by:

$$\nabla^2 \Phi_{total}(x,y,z) = 0 \qquad \ldots (1)$$

where $\Phi_{total}(x,y,z)$ is the total velocity potential comprising of free-stream and induced components. The general solution for Equation (1) can be structured numerically by placing an appropriate distribution of source and doublet flow singularities along the solid body surface S_b[33]. The induced, free-stream, and total potentials at a point $P(x, y, z)$ located within the three-dimensional flow-field are then given by:

$$\Phi_i(x,y,z) = -\frac{1}{4\pi}\int_{S_b} \{\sigma(\frac{1}{r}) - \mu \mathbf{n}\cdot\nabla(\frac{1}{r})\}\mathrm{d}S \qquad \ldots (2)$$

$$\Phi_\infty(x,y,z) = U_\infty x + V_\infty y + W_\infty z \qquad \ldots (3)$$

$$\Phi_{total}(x,y,z) = \Phi_i(x,y,z) + \Phi_\infty(x,y,z) \qquad \ldots (4)$$

where σ and μ are the source and doublet strengths per unit area respectively, r is the effective

https://doi.org/10.1017/S0001924000010563 Published online by Cambridge University Press

geometric distance of the source/doublet from the evaluation point $P(x, y, z)$, and $\mathbf{n}$ is a unit vector perpendicular to dS pointing towards the direction of the potential jump[33].

Imposing the non-penetration condition $\frac{\partial \Phi_{total}}{\partial \mathbf{n}} = 0$ along the solid body surface, essentially results indirectly to the derivation of the Dirichlet boundary condition which dictates constant internal potential within the region enclosed by S_b:

$$\Phi_{total}^{int.} = (\Phi_i + \Phi_\infty)_{body} = c \qquad \ldots (5)$$

where c is an arbitrary constant. Substituting Equation (2) into Equation (5) and subsequently making use of the identity $\mathbf{n} \cdot \nabla f = \frac{\partial f}{\partial \mathbf{n}}$, where f is a scalar function, gives:

$$\Phi_{total}^{int} = \frac{1}{4\pi}\int_{S_b} \mu \frac{\partial}{\partial \mathbf{n}}\left(\frac{1}{r}\right) \mathrm{d}S - \frac{1}{4\pi}\int_{S_b} \sigma\left(\frac{1}{r}\right) \mathrm{d}S + \Phi_\infty = c \qquad \ldots (6)$$

It is noted that the present approach targets the estimation of the induced velocity perturbations of a helicopter fuselage which is assumed to produce zero circulatory lift. Therefore no shed wake effects have been included in the formulation of Equation (6). Setting $c = \Phi_\infty$ in Equation (6) gives:

$$\frac{1}{4\pi}\int_{S_b} \mu \frac{\partial}{\partial \mathbf{n}}\left(\frac{1}{r}\right) \mathrm{d}S - \frac{1}{4\pi}\int_{S_b} \sigma\left(\frac{1}{r}\right) \mathrm{d}S = 0 \qquad \ldots (7)$$

Reference 33 shows that application of the non-penetration condition $\frac{\partial \Phi_{total}}{\partial \mathbf{n}} = 0$ along the solid body boundaries defined by S_b essentially leads to:

$$\sigma = \mathbf{n} \cdot \mathbf{V}_\infty \qquad \ldots (8)$$

Equation (8) expresses the boundary condition used in the present approach for the determination of the source strength per unit area distribution along the fuselage geometry defined by $\mathbf{n}$.

Having assumed that the helicopter fuselage is a bluff body with no circulatory loading and no shed wake, the surrounding flow will only be affected by geometric thickness effects. Thus, placing only source elements along the fuselage geometry, the equation for the induced potential becomes:

$$\Phi_i(x, y, z) = -\frac{1}{4\pi}\int_{S_b} \sigma\left(\frac{1}{r}\right) \mathrm{d}S \qquad \ldots (9)$$

Therefore, the problem can be considered uniquely defined through application of Equation ((8)) in terms of determining the distribution of source strength per unit area over the region defined by S_b. Subsequent evaluation of Equation (9) yields the induced potential at any set of co-ordinates (x, y, z).

Discretising the body geometry into N_p quadrilateral planar panels of constant source strength σ_j, $j = 1, \ldots N_p$ per unit area, leads to the following numerical expression for the analytical Equation (9):

$$\Phi_i(x, y, z) = \sum_{j=1}^{N_p} B_j \sigma_j = 0 \qquad \ldots (10)$$

https://doi.org/10.1017/S0001924000010563 Published online by Cambridge University Press

The coefficient B_j essentially describes the influence of the jth source-panel element at point $P(x, y, z)$ and is defined as follows:

$$B_j = -\frac{1}{4\pi}\int_{S_j}\left(\frac{1}{r}\right)\mathrm{d}S, \quad j = 1,...N \qquad \ldots (11)$$

where S_j is the surface area of the jth panel and r is the geometric distance of point $P(x, y, z)$ from the differential surface element dS. Hess and Smith[34] have provided closed form expressions for the estimation of the induced potential of quadrilateral planar elements with constant source strength and designated end-point co-ordinates. The complete equations are rather lengthy and have also been provided in Ref. 33, hence further elaboration within this paper will be omitted. The co-ordinates of $P(x, y, z)$ can be transformed to the reference frame defined by the planar co-ordinates of the jth panel. This enables the employment of the Hess and Smith expressions[34] for the evaluation of the integral in the right-hand side (RHS) of Equation (11). The velocity perturbations can be subsequently evaluated by estimating the spatial gradient of the induced potential at point $P(x, y, z)$:

$$\mathbf{v} = \nabla\Phi_i \qquad \ldots (12)$$

where $\mathbf{v} = [u, v, w]^T$ is the perturbation velocity vector.

The potential flow method described above is applied to the geometry of the fuselage in order to predict the induced velocity perturbations at the main rotor tip-path plane. Due to the fact that the employed boundary condition (Equation (8)) readily defines the required source strength distribution, there is no need for a numerical solution. This results in the described procedure being very robust and computationally efficient, as well as easy to implement in existing flight dynamics codes.

2.4 Rotor aerodynamics: Modelling of wake-induced flow

2.4.1 Finite-state induced flow modelling approach

The present approach employs the finite-state inflow model of Peters and He[35,36] for the estimation of the unsteady, three-dimensional, wake-induced flow at the rotor tip-path-plane. Contrary to free-wake and prescribed-wake vortex methods, finite-state inflow models employ a continuous wake representation with no associated wake geometry discretisation errors. The original method of Peters and He models the vortical wake as a skewed cylinder without accounting for the effect of self-induced wake roll-up. The induced flow at the rotor disk is expressed as a function of a number of flow-states that are determined by the solution of a first-order ordinary matrix differential equation. Thus, due to their simplicity, finite-state inflow models effectively lend themselves to real-time execution. However, their physical accuracy is dependent on the employed number of flow-states.

The generalised dynamic wake model of Peters and He employs a finite series of normalised associated Legendre functions $\bar{P}_j^r(\nu)$, $\nu = \sqrt{1-\bar{r}^2}$ in order to express the radial distribution of rotor inflow. The azimuthal variation of inflow is described using a Fourier series. Therefore, the normalised wake-induced flow at the rotor disk can be expressed as the sum of an unlimited number of harmonics ($r = 0,1,2\cdots$) and radial shape functions ($j = r+1, r+3\cdots$) as written below:

https://doi.org/10.1017/S0001924000010563 Published online by Cambridge University Press

$$\lambda(\bar{r},\psi,\bar{t}) = \sum_{r=0}^{\infty} \sum_{j=r+1,\ r+3,\ldots}^{\infty} \phi_j^r(\bar{r})[\alpha_j^r(\bar{t})\mathrm{Cos}r\psi + \beta_j^r(\bar{t})\mathrm{Sin}\,r\psi] \quad \ldots(13)$$

where $\bar{r}$ is the local non-dimensional radial location ($\bar{r} = (r/R$, R being the rotor blade radius), $\bar{t}$ is the non-dimensional time ($\bar{t} = \Omega t$, Ω being the shaft rotor speed), ψ denotes the azimuthal co-ordinate on the rotor disk, and $\phi_j^r(\bar{r}) = \bar{P}_j^r(v)/v$. The model's flow-states essentially correspond to the time-dependent scalar coefficients for the cosine and sine harmonic terms in the RHS of Equation (13), $\alpha_j^r(\bar{t})$ and $\beta_j^r(\bar{t})$, respectively. These are determined by the solution of the following linear systems of first-order ODEs:

$$\mathbf{M}^{\mathbf{c}}\{\dot{\alpha}_j^r\} + \mathbf{V}^{\mathbf{c}}\mathbf{L}^{\mathbf{c}-1}\{\alpha_j^r\} = \frac{1}{2}\{\tau_n^{mc}\} \quad \ldots(14)$$

$$\mathbf{M}^{\mathbf{s}}\{\dot{\beta}_j^r\} + \mathbf{V}^{\mathbf{s}}\mathbf{L}^{\mathbf{s}-1}\{\beta_j^r\} = \frac{1}{2}\{\tau_n^{ms}\} \quad \ldots(15)$$

where $\mathbf{M^c}$ and $\mathbf{M^s}$ are the apparent mass matrices that contain the time-constants associated with the cosine and sine matrix ODEs described by Equation (14) and Equation (15), respectively. Similarly, $\mathbf{L^c}$ and $\mathbf{L^s}$ are the cosine and sine inflow gain matrices, in that order. These depend only on the wake skew parameter $X, X = \mathrm{Tan}\,|\chi/2|$ where χ is the wake skew angle), whilst $\mathbf{V^c}$ and $\mathbf{V^s}$ denote the mass flow parameter matrices for the corresponding parts of the matrix ODEs. The described matrices required for the implementation of the Peters and He model have been provided in Refs 35 and 36. The pressure coefficients in the RHS of Equations (14) and (15), and $\boldsymbol{\tau}_n^{mc}$, $\boldsymbol{\tau}_n^{ms}$ are user-supplied integrals denoting the generalised aerodynamic forces on the rotor disk. These depend only on the circulatory blade lift and can be obtained using any aerodynamic theory.

Thus, the Peters and He model constitutes a generalised dynamic wake theory that is capable of providing the unsteady wake-induced flow at the rotor disk. Furthermore, it is compatible with any aerodynamic theory that can provide the circulation developed by the rotor blades. However, Equations (14) and (15) still treat the rotor wake as a skewed cylinder without any account for wake distortion effects such as curvature, vortex spacing, or wake roll-up. Further elaboration on the theoretical development and validation of finite-state induced flow models, as well as a comprehensive description of the current 'state of the art' is provided in Refs 37-39.

2.4.2 Modelling of rotor wake distortion

It is well known that for a typical helicopter pull-up manoeuver there is inevitably an associated roll response (an off-axis response) and vice versa. It has been shown in Ref. 40 that this effect originates in the effective curvature of the rotor wake during maneuvering flight. Due to the pitch/roll angular motion of the shaft the wake essentially distorts into a curved helix. Hence, the blade tip-vortices effectively pile-up more tightly beneath one semicircle of the rotor disk, while synchronously expand more quickly downstream of the blades on the opposite side of the disk. This leads to first harmonic inflow gradients that produce a cyclic pitch effect, thus forcing the blades close to their fundamental flap frequency. The blades respond to once-per-rev (1P) harmonic forcing with a phase lag of approximately 90º, therefore generating hub moments in an off-axis manner.

A numerical approach similar to the one proposed originally by Krothapalli[41] and Krothapalli *et al*[42] is used in this paper to augment the generalised dynamic wake model of Peters and He, in order to account for the effect of rotor wake curvature. The augmented model is written as follows:

https://doi.org/10.1017/S0001924000010563 Published online by Cambridge University Press

$$\begin{bmatrix} \mathbf{M}^c & 0 \\ 0 & \mathbf{M}^s \end{bmatrix} \begin{Bmatrix} \dot{\alpha}_j^r \\ \dot{\beta}_j^r \end{Bmatrix} + \begin{bmatrix} \mathbf{V}^c & 0 \\ 0 & \mathbf{V}^s \end{bmatrix} \left\{ \begin{bmatrix} \mathbf{L}^c & 0 \\ 0 & \mathbf{L}^s \end{bmatrix} + K_{Re} \quad \mathbf{C} \right\}^{-1} \begin{Bmatrix} \alpha_j^r \\ \beta_j^r \end{Bmatrix} = \frac{1}{2} \begin{Bmatrix} \tau_n^{mc} \\ \tau_n^{ms} \end{Bmatrix} \quad \ldots (16)$$

where the matrices $\mathbf{M}^{c/s}$, $\mathbf{L}^{c/s}$, $\mathbf{V}^{c/s}$ are the original apparent mass, inflow gain, and mass flow parameter matrices, respectively, as employed in Equations (14) and (15) of the original Peters and He model. The terms K_{Re} and $\mathbf{C}$ essentially denote the wake curvature parameter[42] and the corresponding matrix of influence coefficients, respectively. In the original model of Krothapalli[42], the wake curvature influence matrix $\mathbf{C}$ depends only on the longitudinal and lateral wake curvature values, κ_c and κ_s, respectively. For quasi-steady conditions, κ_c and κ_s can be written as shown below:

$$\kappa_c = \frac{\bar{q} - \bar{\dot{\beta}}_{1c}}{\lambda_m + \lambda_f} \quad \ldots (17)$$

$$\kappa_s = \frac{\bar{p} - \bar{\dot{\beta}}_{1s}}{\lambda_m + \lambda_f} \quad \ldots (18)$$

where $\bar{q}$ and $\bar{p}$ signify the normalised pitch and roll rates, respectively, whilst $\bar{\dot{\beta}}_{1c}$ and $\bar{\dot{\beta}}_{1s}$ denote the normalised rates of first harmonic flapping ($\frac{\dot{\beta}_{1c}}{\Omega}$ and $\frac{\dot{\beta}_{1s}}{\Omega}$). λ_f and λ_m refer to the normalised free-stream and mean induced flow, in that order. The derivation of the wake curvature influence matrix is described in Refs 42 and 43 for near-hover $\mathbf{C}$ and forward flight $\mathbf{D}$, respectively.

It can be observed from Equation (16) that after including the effect of wake curvature in the overall finite-state model, the inflow gain matrices obtained from the original formulation of Peters and He, $\mathbf{L}^c$ and $\mathbf{L}^s$, are now combined into a single partitioned inflow gain matrix. This is due to the fact that wake curvature essentially introduces a coupling between the mean disk loading and the longitudinal as well as lateral variations of induced flow. It is noted that in the original model of Peters and He (Equations (14) and (15)), coupling exists only between the mean disk loading and the longitudinal gradient of inflow which is due to the non-zero wake skew angle in forward flight.

Furthermore, Prasad *et al*[44,45] showed that in the same way that dynamic inflow incurs a first-order time-delay in the development of the wake-induced flow, the effects of longitudinal and lateral wake curvature (κ_c and κ_s), along with vortex spacing $S = 2\pi V_T$, $V_T = \sqrt{\bar{\mu}^2 + (\lambda_f + \lambda_m)^2}$ and wake skew X, also exhibit first-order behaviour with respect to non-dimensional time $\bar{t}$. Hence, their time-dependent nature can be modelled using a system of first-order ODEs. Zhao[43] employed a numerical approach based on the vortex tube analysis in order to extract the respective time-delays for the aforementioned parameters of wake distortion. In doing so, Zhao developed a four-state reduced order model that can be expressed in the following form:

$$\begin{bmatrix} \tau_X & 0 & 0 & 0 \\ 0 & \tau_S & 0 & 0 \\ 0 & 0 & \tau_R & 0 \\ 0 & 0 & 0 & \tau_R \end{bmatrix} \begin{Bmatrix} \dot{X} \\ \dot{S} \\ \dot{\kappa}_c \\ \dot{\kappa}_s \end{Bmatrix} + \begin{Bmatrix} X \\ S \\ \kappa_c \\ \kappa_s \end{Bmatrix} = \begin{Bmatrix} X \\ S \\ \kappa_c \\ \kappa_s \end{Bmatrix}_{qs} \quad \ldots (19)$$

where the subscript $(\,)_{qs}$ denotes quasi-steady conditions whilst τ_X, τ_S, and τ_R are the time-constants associated with the dynamic behaviour of wake skew, vortex spacing, and wake curvature, respectively. These have been provided by Zhao *et al* as functions of the mass flow parameter associated with the first and higher-order harmonics of rotor inflow in Refs 43 and 46.

https://doi.org/10.1017/S0001924000010563 Published online by Cambridge University Press

The Zhao-Prasad dynamic wake distortion model (Equation (19)) has been numerically coupled with the Peters-He induced-flow model (Equations (14) and (15)) using the wake curvature augmentation method for hover (**C** and forward flight (**D**), expressed by Equation (16). The combined fluid dynamics formulation is utilised within this paper for the prediction of wake-induced flow including the unsteady aerodynamic effects of wake curvature, skew, and vortex spacing.

2.4.3 Coupled aeroelastic rotor-fuselage model

The employed rotor dynamics model[28-30] in combination with the finite-state induced flow formulation of Peters-He[35,36] and the wake distortion approach of Zhao-Prasad[46,47], have been coupled with the Leishman-Beddoes unsteady nonlinear aerodynamics model[48]. Experimentally derived quasi-steady aerofoil data extracted from Ref. 49, are incorporated for the calibration of the Leishman-Beddoes model. Careful treatment of the induced flow terms arising from shed wake circulation has been carried out so that they are not duplicated by both induced flow and unsteady aerodynamics models. The dynamic response of the elastic blades to external forcing is calculated using a fifth-order accurate numerical evaluation scheme of the convolution integral.

The numerical approach employed in this study makes use of the assumption that the fuselage induced velocity perturbations can be superimposed on the main rotor inflow. The implications of rotor wake distortion due impingement on the aircraft fuselage are not catered for. However, the effect of an altered time-history of circulatory blade loading due to the presence of the fuselage, is captured implicitly through the formulation of the Peters-He inflow model. For the range of flight conditions that wake impingement on the fuselage occurs, a time-averaged induced velocity profile over the rotor disc is considered. This velocity profile is superimposed upon the free-stream components encountered by the discretised fuselage panel model. The superposition is applied at the appropriate panel locations depending on the wake skew angle relative to the fuselage. Larger wake skew angles dictate that the wake does not impinge on the fuselage and therefore only the free-stream component is accounted for.

2.5 Helicopter flight dynamics: Mathematical model development

2.5.1 Rigid body fuselage kinematics

Reference 24 presented the derivation of the equations of motion for the six fuselage DOFs, expressed in the respective axes system. The derivation was carried out by applying Newton's laws of motion relating the applied forces and moments to the resulting translational and angular accelerations of the fuselage. The equations of motion were presented in the following form:

$$\dot{u} = -(w \cdot q - v \cdot r) + \frac{X}{M_a} - g \cdot \mathrm{Sin}\,\Theta \qquad \ldots (20)$$

$$\dot{v} = -(u \cdot r - w \cdot p) + \frac{Y}{M_a} + g \cdot \mathrm{Cos}\,\Theta \cdot \mathrm{Sin}\,\Phi \qquad \ldots (21)$$

$$\dot{w} = -(v \cdot p - u \cdot q) + \frac{Z}{M_a} + g \cdot \mathrm{Cos}\,\Theta \cdot \mathrm{Cos}\,\Phi \qquad \ldots (22)$$

$$\dot{p} = \frac{I_{yy} - I_{zz}}{I_{xx}} \cdot q \cdot r + \frac{I_{xz}}{I_{xx}} \cdot (\dot{r} + p \cdot q) + \frac{L}{I_{xx}} \qquad \ldots (23)$$

https://doi.org/10.1017/S0001924000010563 Published online by Cambridge University Press

$$\dot{q} = \frac{I_{zz} - I_{xx}}{I_{yy}} \cdot r \cdot p + \frac{I_{xz}}{I_{yy}} \cdot (r^2 - p^2) + \frac{M}{I_{yy}} \quad \ldots (24)$$

$$\dot{r} = \frac{I_{xx} - I_{yy}}{I_{zz}} \cdot p \cdot q + \frac{I_{xz}}{I_{zz}} \cdot \left|(\dot{p} - q \cdot r) + \frac{N}{I_{zz}}\right. \quad \ldots (25)$$

$$\dot{\Phi} = p + q \cdot \mathrm{Sin}\,\Phi \cdot \mathrm{Tan}\,\Theta + r \cdot \mathrm{Cos}\,\Phi \cdot \mathrm{Tan}\,\Theta \quad \ldots (26)$$

$$\dot{\Theta} = q \cdot \mathrm{Cos}\,\Phi - r \cdot \mathrm{Sin}\,\Phi \quad \ldots (27)$$

$$\dot{\Psi} = q \cdot \mathrm{Sin}\,\Phi \cdot \mathrm{Sec}\,\Theta + r \cdot \mathrm{Cos}\,\Phi \cdot \mathrm{Sec}\,\Theta \quad \ldots (28)$$

where u, v, w and p, q, r signify the aircraft's linear and angular velocity components, respectively. These are effectively expressed about the aircraft centre of gravity (CG) in the fuselage frame of reference, as shown in Fig. 19(a). Furthermore, Θ, Φ and Ψ are the fuselage pitch, roll and yaw attitude angles, respectively, whilst M_a and g correspond to the fuselage mass and the gravitational constant. The elements I_{xx}, I_{yy} and I_{zz} denote the roll, pitch, and yaw moments of inertia of the fuselage, in that order. The component I_{xz} signifies the roll-yaw cross-coupling moment of inertia. The symbols X, Y, Z, L, M and N denote the individual components of the three-dimensional forces and moments that are applied externally about the aircraft CG. These are also expressed in the fuselage axes reference frame and essentially include the contribution of each rotorcraft component; main rotor, tail-rotor, empennage, as well as any aerodynamic loads generated by the fuselage itself.

Equations (20)-(28) constitute a system of first-order ODEs where the forcing functions essentially comprise the external (aerodynamic) forces and moments applied about the aircraft CG (X, Y, Z, L, M, N). It can be observed that the roll and yaw accelerations ($\dot{p}$ and $\dot{r}$; Equations (23) and (25)) are implicitly coupled through the roll-yaw cross-coupling moment of inertia I_{xz}. This inertial coupling is substantial for modern helicopter fuselage designs. As an example, it is noted that I_{xz} reaches approximately 43% of the roll moment of inertia I_{xx} for the case of the Bo105 helicopter. Hence, this inertial coupling needs to be accounted for in modern flight dynamics simulation models.

The form of Equations (20)-(28) in which they were provided in Ref. 24, does not allow the deployment of explicit numerical methods for direct time-integration. This is due to the implicit coupling between $\dot{p}$ and $\dot{r}$ which dictates that $\dot{p} = f(\dot{r})$ and $\dot{r} = g(\dot{p})$, as shown in Equations (23) and (25). This effectively leads to; $\dot{p} = f(g(\dot{p})) \Rightarrow \dot{p} = R(\dot{p})$. Similarly, it also follows that; $\dot{r} = g(f(\dot{r})) \Rightarrow \dot{r} = L(\dot{r})$. This implicit coupling in the roll-yaw equations may lead to an instability during nonlinear control response simulation where Equations (20)-(28) need to be continuously integrated numerically in the time-domain. This instability appears due to accumulating numerical errors in the time-integration of Equations (23) and (25). This effect manifests when the employed values of $\dot{p}$ and $\dot{r}$ in the RHS of Equations (23) and (25) at time = t are obtained from the previous time-step ($t - \Delta t$), when in fact they refer to the present values (t) that are effectively unknown.

Hence, Equations (23) and (25) are re-formulated in order to mitigate the implicit coupling between the roll-yaw DOFs and re-derive a set of equations that are essentially free of such numerical instabilities. This process is carried out by expressing Equations (23) and (25) in the form of 2 x 2 linear system of equations with constant coefficients, where $\dot{p}$ and $\dot{r}$ constitute the unknown variables. Analytical solution of the linear system, after some careful mathematical

https://doi.org/10.1017/S0001924000010563 Published online by Cambridge University Press

manipulations that are omitted in this paper for brevity, results in a set of compact closed form expressions for the unknown variables $\dot{p}$ and $\dot{r}$. These are given as sole functions of the equations' coefficients. The final expressions are written as:

$$\dot{p} = f_1 \cdot p \cdot q + f_2 \cdot q \cdot r + f_3 \cdot N + f_4 \cdot L \quad \ldots (29)$$

$$\dot{r} = k_1 \cdot p \cdot q + k_2 \cdot q \cdot r + k_3 \cdot N + k_4 \cdot L \quad \ldots (30)$$

where the coefficients $k_{1\text{-}4}$ and $f_{1\text{-}4}$ are given by the following closed form expressions:

$$k_1 = \frac{I_{xx} - I_{yy} + \frac{I_{xz}^2}{I_{xx}}}{I_{zz} - \frac{I_{xz}^2}{I_{xx}}} \quad \ldots (31)$$

$$k_2 = \frac{\frac{I_{yy} - I_{zz}}{I_{xx}} - 1}{\frac{I_{zz}}{I_{xz}} - \frac{I_{xz}}{I_{xx}}} \quad \ldots (32)$$

$$k_3 = \frac{I_{xx}}{I_{xx} \cdot I_{zz} - I_{xz}^2} \quad \ldots (33)$$

$$k_4 = \frac{I_{xz}}{I_{xx} \cdot I_{zz} - I_{xz}^2} \quad \ldots (34)$$

$$f_1 = \frac{I_{xz} \cdot (1 + k_1)}{I_{xx}} \quad \ldots (35)$$

$$f_2 = \frac{I_{yy} - I_{zz} + I_{xz} \cdot k_2}{I_{xx}} \quad \ldots (36)$$

$$f_3 = \frac{I_{xz} \cdot k_3}{I_{xx}} \quad \ldots (37)$$

$$f_4 = \frac{1 + I_{xz} \cdot k_4}{I_{xx}} \quad \ldots (38)$$

It can be observed that Equations (29) and (30) relate the roll-yaw accelerations, $\dot{p}$ and $\dot{r}$, with the respective angular rates (p, q and r) in a fully explicit manner. As such, the described transformation has effectively mitigated the implicit coupling in the roll-yaw accelerations, that was previously noted in Equations (23) and (25). It is emphasised that no assumption has been made considering the nature of the implicitly coupled equations during the aforementioned mathematical transformation. As such, the quality of the original ODEs has not been altered or compromised in any way. Equations (29), (30) can replace Equations (23) and (25) in the ODE system described

https://doi.org/10.1017/S0001924000010563 Published online by Cambridge University Press

by Equations (20)-(28). This results in an explicit set of first-order ODEs which describes the rigid-body kinematics of the fuselage and can be utilised by existing flight dynamics codes for nonlinear trim, stability and control response analyses. The complete transformed system of first-order ODEs is written below for consistency:

$$\dot{u} = -(w \cdot q - v \cdot r) + \frac{X}{M_a} - g \cdot \mathrm{Sin}\,\Theta \quad \ldots (39)$$

$$\dot{v} = -(u \cdot r - w \cdot p) + \frac{Y}{M_a} + g \cdot \mathrm{Cos}\,\Theta \cdot \mathrm{Sin}\,\Phi \quad \ldots (40)$$

$$\dot{w} = -(v \cdot p - u \cdot q) + \frac{Z}{M_a} + g \cdot \mathrm{Cos}\,\Theta \cdot \mathrm{Cos}\,\Phi \quad \ldots (41)$$

$$\dot{p} = f_1 \cdot p \cdot q + f_2 \cdot q \cdot r + f_3 \cdot N + f_4 \cdot L \quad \ldots (42)$$

$$\dot{q} = \frac{I_{zz} - I_{xx}}{I_{yy}} \cdot r \cdot p + \frac{I_{xz}}{I_{yy}} \cdot (r^2 - p^2) + \frac{M}{I_{yy}} \quad \ldots (43)$$

$$\dot{r} = k_1 \cdot p \cdot q + k_2 \cdot q \cdot r + k_3 \cdot N + k_4 \cdot L \quad \ldots (44)$$

$$\dot{\Phi} = p + q \cdot \mathrm{Sin}\,\Phi \cdot \mathrm{Tan}\,\Theta + r \cdot \mathrm{Cos}\,\Phi \cdot \mathrm{Tan}\,\Theta \quad \ldots (45)$$

$$\dot{\Theta} = q \cdot \mathrm{Cos}\,\Phi - r \cdot \mathrm{Sin}\,\Phi \quad \ldots (46)$$

$$\dot{\Psi} = q \cdot \mathrm{Sin}\,\Phi \cdot \mathrm{Sec}\,\Theta + r \cdot \mathrm{Cos}\,\Phi \cdot \mathrm{Sec}\,\Theta \quad \ldots (47)$$

Equations (39)-(47) can be evaluated numerically in the context of nonlinear control response simulation using explicit time-integration techniques, without any potential instabilities due to the implicit coupling between the roll-yaw acceleration terms, $\dot{p}$ and $\dot{r}$, respectively.

2.5.2 Integrated aeroelastic rotor-aircraft model

The aircraft fuselage is treated dynamically as a rigid body with six degrees of freedom (three translations and three rotations) using the inertial tensor and mass value (M_a) provided in Ref. 24. Experimentally derived look-up tables extracted from Ref. 24, are also employed for the estimation of fuselage force and moment coefficients as functions of incidence and sideslip angles. Look-up tables are utilised for the prediction of the aerodynamic behaviour of the horizontal and vertical stabilisers. Steady-state two-dimensional aerofoil characteristics along with a first-order dynamic inflow[50-52] are used for the prediction of tail-rotor performance. Rigid body dynamics are employed for the simulation of the dynamic behaviour of the tail-rotor blades.

A globally convergent Newton-Raphson method is incorporated in order to obtain rotor trim for a designated set of flight conditions. The numerical scheme is used for the solution of Equations (39)-(47) using matching constraints that require zero translational and angular accelerations

https://doi.org/10.1017/S0001924000010563 Published online by Cambridge University Press

for the aircraft fuselage. The main and tail rotors are marched simultaneously in time using the initial condition of nonexistent circulatory wake. The time-marching process continues until a once-per-rev (1P) periodic condition is achieved with respect to the main rotor mean and first harmonic multi-blade co-ordinates (MBCs) of flap (β_0, β_{1c}, β_{1s}) and lead-lag motion (ζ_0, ζ_{1c} and ζ_{1s}), respectively. For the blade flapping case the MBCs are defined in the non-rotating global O reference frame as follows:

$$\beta_0(t) = \frac{1}{N_b}\sum_{i=1}^{N_b}\beta(R,t) \quad \ldots (48)$$

$$\beta_{1c}(t) = \frac{2}{N_b}\sum_{i=1}^{N_b}\beta(R,t)\cdot \mathrm{Cos}\,\psi_i(t) \quad \ldots (49)$$

$$\beta_{1s}(t) = \frac{2}{N_b}\sum_{i=1}^{N_b}\beta(R,t)\cdot \mathrm{Sin}\,\psi_i(t) \quad \ldots (50)$$

where N_b is the number of the rotor blades and $\psi_i(t)$ is the azimuth angle of each blade ($i = 1, \cdots N_b$) at time = t. Similar expressions are used for the respective MBCs in the lead-lag case; ζ_0, ζ_{1c} and ζ_{1s}. Having achieved periodicity in the aeroelastic rotor response, a finite series of rotations is carried out where the rotor loads are averaged in time to acquire mean values to be used for trim.

Estimation of S & C derivatives is conducted by numerically perturbing the integrated aeroelastic rotor-aircraft model around an acquired trim condition. Extraction of perturbation forces and moments is carried out when 1P periodicity is achieved with respect to the main rotor flap/lag MBCs. The corresponding S & C derivatives are subsequently calculated using second-order central finite-differences. Simulation of nonlinear control response is carried out after obtaining rotor trim by applying a pre-defined schedule of control inputs. Fourth-order accurate Runge-Kutta integration is deployed in order to integrate Equations (39)-(47) in the fuselage axes system.

3.0 RESULTS AND DISCUSSION

The developed source-panel potential flow method is initially applied to the isolated ROBIN fuselage. The proposed approach is validated with experimental measurements in terms of steady-state induced velocity perturbations at the imaginary rotor plane. Subsequently, the described flight dynamics simulation model is deployed in order to investigate the effects of rotor-fuselage interaction on trim, stability, control response, and oscillatory structural blade loads for a full-scale helicopter modelled after the Eurocopter Bo105. The natural vibration characteristics of the hingeless rotor blades of the Bo105 helicopter were analysed with the author's Lagrangian formulation[26] in Ref. 29 using the structural properties of the blade reported in Ref. 53. The modal content presented in Ref. 29 is utilised within this paper for the estimation of the rotor blade's dynamic response to nonlinear external forcing.

Unless indicated otherwise, a total of eight inflow harmonics were deployed in order to capture the effect of higher harmonic loading on rotor inflow response. The respective radial inflow distribution polynomials used, reached up to the tenth power of non-dimensional rotor radius. This inflow model configuration resulted in a dynamic-wake representation of 62 states. Six vibration modes were employed for each blade DOF, along with 900 quadrilateral planar panels of constant strength for the numerical discretisation of the fuselage geometry.

https://doi.org/10.1017/S0001924000010563 Published online by Cambridge University Press

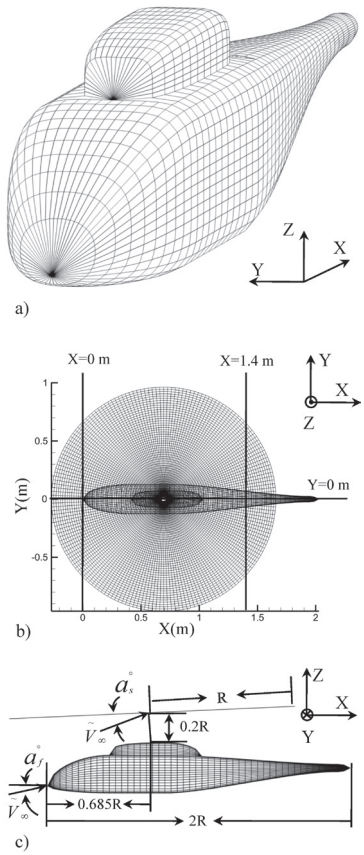

Figure 1. ROBIN fuselage geometry: (a) Three-dimensional panel model - Global reference system, (b) Comparison lines location on rotor disc (X = 0m, X = 1·4m, and Y = 0), (c) Definition of rotor shaft and fuselage incidence angles (α_s and α_f respectively).

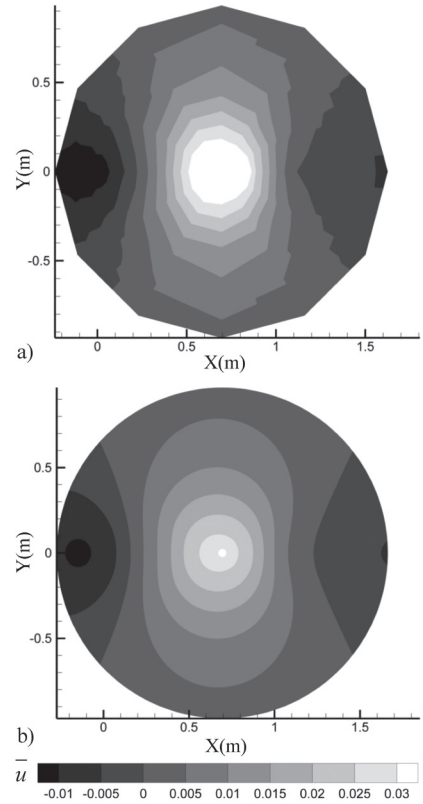

Figure 2. Longitudinal induced velocity perturbation component tangential to the main rotor disc, $\bar{u}$: (a) Measurements reported in Ref. 5, (b) Simulation.

Simulation results are presented for a wide range of advance ratios ($\bar{\mu} = \frac{V_{flight}}{\Omega R}$). Predictions of oscillatory structural blade loads are compared with experimental data from flight test measurements reported in Ref. 54. Correlations are conducted with system identification results reported in Refs 55-57, in terms of trim parameters, S & C derivatives, and nonlinear response to pilot control inputs. With reference to the structural blade loads correlations, the main rotor was numerically trimmed to prescribed values of thrust and hub moments for a given advance ratio and shaft angle relative to the free-stream flow. This was done in order for the simulations to comply with the flight testing procedures reported in Ref. 54.

3.1 Induced velocity perturbations from an isolated helicopter fuselage in a free-stream

Figure 1(a) illustrates the ROBIN fuselage geometry which was employed for the computations of induced velocity perturbations presented in this section. Comparisons are presented

https://doi.org/10.1017/S0001924000010563 Published online by Cambridge University Press

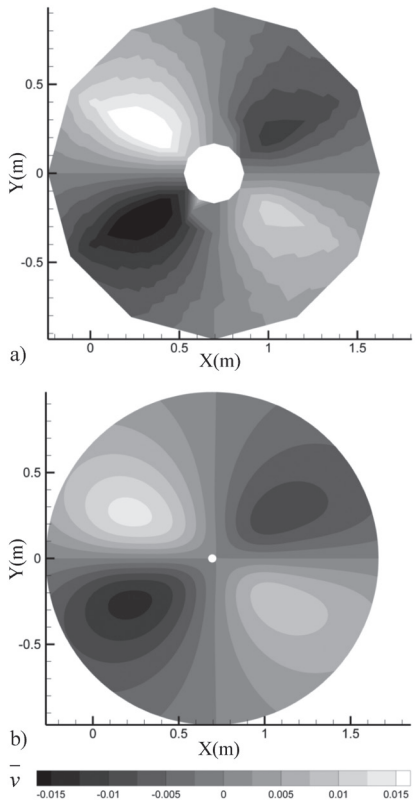

Figure 3. Lateral induced velocity perturbation component tangential to the main rotor disc, $\bar{v}$: (a) Measurements reported in Ref. 5, (b) Simulation.

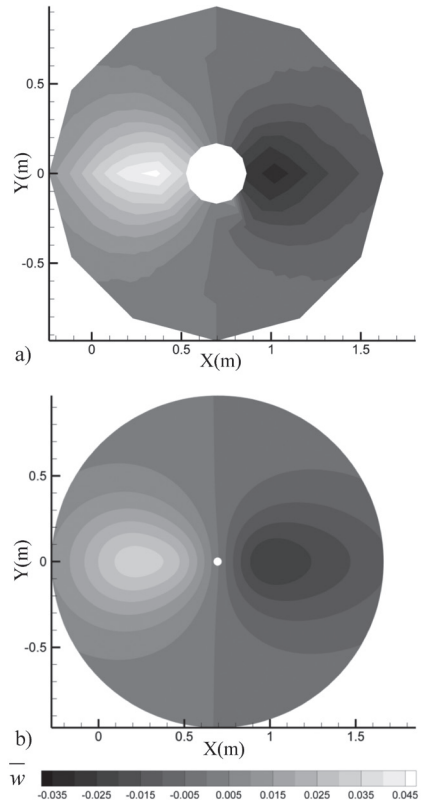

Figure 4. Induced velocity perturbation component normal to the rotor disc, $\bar{w}$: (a) Measurements reported in Ref. 5(b) Simulation.

with experimental data extracted from Ref. 5, regarding the induced flow-field conditions at the imaginary rotor tip-path plane for the isolated fuselage. It is noted that the fuselage geometry used for the experiments reported in Ref. 5 includes a slender portion of the rotor shaft including the rotor hub. However, the aforementioned components were not modelled in the present analysis.

Results are presented for a free-stream velocity of $|\mathbf{V}_\infty|$ = 28·65 m/sec with a fuselage incidence of α_f = –0·5° nose down. The imaginary rotor tip-path plane incidence was α_s = –3°. The exact test conditions were described in Ref. 5. The rotor plane position relative to the fuselage body is illustrated in Figs 1(b) and (c). All dimensions are provided as functions of an effective rotor blade radius (R = 1·014m) which corresponds to the scale of the experimental model. One longitudinal (at Y = 0m) and two lateral reference lines (at X = 0m and X = 1·4m, respectively) were defined along the imaginary rotor tip-path plane as shown in Fig. 1(b), for which the computed variations of velocity perturbations were compared with measured data.

Figures 2-4 present qualitative comparisons between predicted and measured values of normalised induced velocity perturbations ($\bar{u}$, $\bar{v}$, $\bar{w}$) on the main rotor tip-path plane. The normalised perturbation velocities are defined as follows:

$$\bar{u} = \frac{u \operatorname{Cos}\alpha_s - w \operatorname{Sin}\alpha_s}{|\mathbf{V}_\infty|} \qquad \ldots (51)$$

https://doi.org/10.1017/S0001924000010563 Published online by Cambridge University Press

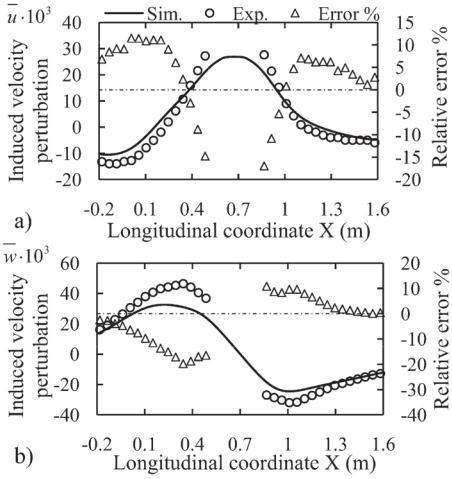

Figure 5. Longitudinal variation of induced velocity perturbations for Y = 0m - Comparison with measured data reported in Ref. 5: (a) Tangential component $\bar{u}$:, (b) Normal component $\bar{w}$:

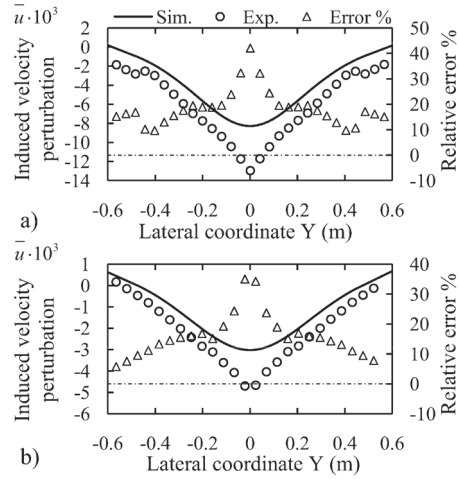

Figure 6. Lateral variation of induced velocity perturbation component $\bar{u}$ - Comparison with measured data reported in Ref.5: (a) X = 0m, (b) X = 1.4m.

$$\bar{v} = \frac{v}{|\mathbf{V}_\infty|} \quad \ldots (52)$$

$$\bar{w} = \frac{w\mathrm{Cos}\,\alpha_s + u\,\mathrm{Sin}\,\alpha_s}{|\mathbf{V}_\infty|} \quad \ldots (53)$$

It is noted that good qualitative correlation is exhibited for all perturbation components between numerical results and measured data. Figures 2(a) and (b) show a strong value of $\bar{u}$ directly over the imaginary rotor head. Figures 3(a) and (b) indicate a pattern where the flow is influenced by the initial lateral divergence around the fuselage geometry and subsequent convergence as the fuselage thickness goes to zero at the tail. Figures 4(a) and (b) reveal a strong up-wash starting at the leading edge of the rotor disc, followed by a down-wash ending at the disc trailing edge.

Figures 5(a) and (b) present comparisons between simulations (Sim.) and experimental measurements (Exp.) for the longitudinal variations of $\bar{u}$ and $\bar{w}$ velocity perturbations, respectively. Results are presented for the reference line corresponding to Y = 0m as shown in Fig. 1(b). The percentage relative error (Rel. error % = $100 \cdot \dfrac{\bar{u}_{sim} - \bar{u}_{exp}}{\left|\bar{u}_{exp}^{max} - \bar{u}_{exp}^{min}\right|}$ similarly for $\bar{v}$ and $\bar{w}$) between numerical predictions and experimental measurements is also shown (Error %) in order to quantify the accuracy of the proposed approach. Good agreement can be observed for both velocity perturbations away from the vicinity close to the imaginary rotor hub ($X \approx 0{\cdot}7$m). The relative error for $\bar{w}$ is consistently in the range of ±4% for the radially outward locations. A small underprediction of $\bar{u}$ can be noted in the region close to the rotor disc leading edge ($X \approx -0{\cdot}2$m), with a relative error

https://doi.org/10.1017/S0001924000010563 Published online by Cambridge University Press

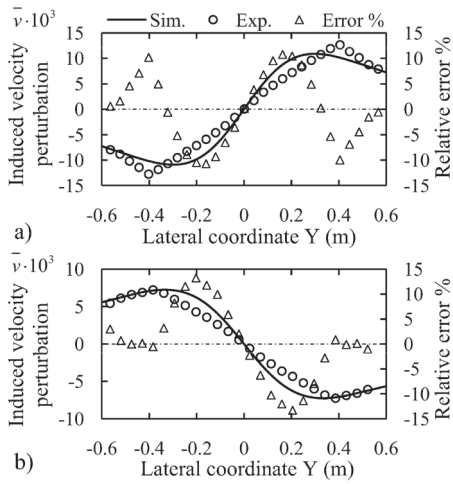

Figure 7. Lateral variation of induced velocity perturbation component $\bar{v}$ - Comparison with measured data reported in Ref. 5: (a) X = 0m, (b) X = 1·4m.

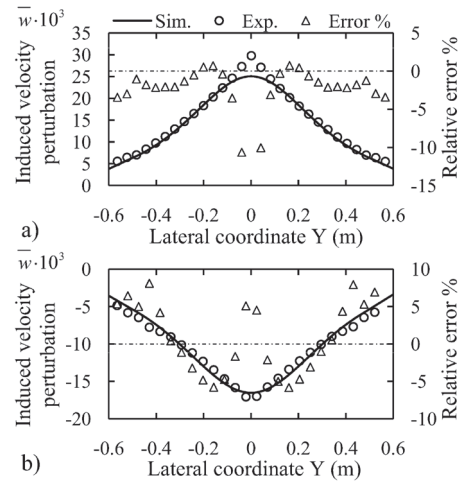

Figure 8, Lateral variation of induced velocity perturbation component $\bar{w}$ - Comparison with measured data reported in Ref. 5: (a) X = 0m, (b) X = 1·4m.

of the order of 5-10%. However, the prediction error in the region close to the rotor hub reaches approximately –15% (±10% for $\bar{w}$). This discrepancy is attributed to the absence of the rotor shaft and hub components in the modelled geometry (Fig. 1(a)). Deviations observed aft of the rotor hub are also due to a large amount of unmodelled separated flow within this region, as noted in Ref. 5. The relative error for $\bar{u}$ in the vicinity close to the disk trailing edge ($X \approx 1{\cdot}6$m) is roughly 3%.

Figures 6-8 present quantitative comparisons between numerical predictions and experimental measurements of the lateral variations of induced flow perturbations $\bar{u}$, $\bar{v}$, and $\bar{w}$, respectively. Results are presented for the reference lines corresponding to X = 0m (Figs 6-8(a)) and X = 1·4m (Figs 6-8(b)). A consistent underprediction of $\bar{u}$ close to the rotor disc leading edge (X = 0m) is observed in Fig. 6(a), although the perturbation gradient is accurately captured. The corresponding relative error is consistently between 10% and 20%, although an overshoot of approximately 40% is observed in the region directly ahead of the rotor hub ($Y \approx 0$). A similar behaviour is also observed in Fig. 6(b) with regards to the position close to the disc trailing edge (X = 1·4m). This is again due the absence of the actual rotor hub components in the modelled fuselage geometry, as shown in Fig. 1(a).

Figures 7(a) and (b) show that the nature of $\bar{v}$ perturbation is well predicted for both longitudinal locations, although the simulations suggest steeper lateral inflow gradients for both longitudinal reference lines. The relative error for $\bar{v}$, is consistently within ±10% and ±15% for X = 0 and X = 1·4, respectively. Very good prediction of $\bar{w}$ is demonstrated for both longitudinal co-ordinates in Figs 8(9a) and 9(b). The respective values of relative error are roughly of the order of –3% and ±5% for X = 0m and X = 1·4m, respectively. The overshoots of error observed in the vicinity close to Y = 0m, are attributed to the absence of the rotor hub in the modelled geometry.

It is noted that the dominant perturbation component that affects the aerodynamic forces exerted on the rotor blades, is the one normal to the rotor tip-path plane ($\bar{w}$). The remaining perturbations which essentially influence the tangential velocity encountered by the blades, are rather insignificant compared to the rotational and free-stream components, particularly for radially outwards

https://doi.org/10.1017/S0001924000010563 Published online by Cambridge University Press

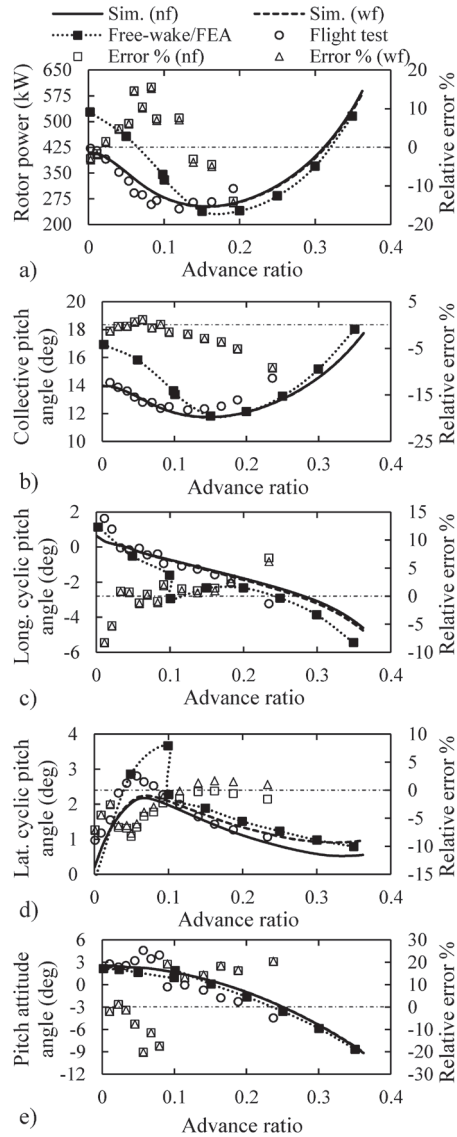

Figure 9. Effects of fuselage induced flow on the Bo105 helicopter trim – Comparison with flight test data[55] and free-wake/FEA results[25]: a) Rotor power required P_{rotor}, b) Collective pitch angle θ_0, (c) Longitudinal cyclic pitch angle θ_{1s}, d) Lateral cyclic pitch angle θ_{1c}, e) Fuselage pitch attitude angle Θ.

locations. The normal perturbation component induced by the fuselage can be of considerable magnitude when compared to the flow induced by the rotor wake, especially considering high-speed flight conditions where the latter is drastically reduced. It was shown in Figs 5(b) and Fig. 8 that the behaviour of $\bar{w}$ was fairly accurately captured away from the vicinity close to the rotor hub. Thus, the described numerical approach can be used with confidence in order to assess the effects of fuselage induced velocity perturbations on the aeroelastic response of the main rotor.

https://doi.org/10.1017/S0001924000010563 Published online by Cambridge University Press

3.2 Effects of fuselage aerodynamic interference on helicopter trim

Figure 9 presents results from nonlinear trim simulations performed for the Bo105 helicopter using the real-time flight dynamics model described in this paper. Results are presented as functions of advance ratio from hover ($\bar{\mu} = 0$) to high-speed flight ($\bar{\mu} = 0{\cdot}36$). Simulations were carried out with the inclusion of fuselage aerodynamic interference effects as well as without. Comparisons with flight test data[55] and predictions made with a high-complexity flight dynamics simulation code[25] are also shown. The simulation method of Ref. 25 is a non-real time formulation employing advanced technologies. Elastically and inertially coupled modal properties obtained from nonlinear finite element analysis (FEA) are used for the structural representation of the elastic blades. A relaxation-type free-wake model is employed for the prediction of wake induced flow, thus accounting for the roll-up of the tip vortices downstream of the rotor blades. However, the aerodynamic interaction between the main rotor and fuselage is not accounted for in the overall analysis.

The percentage errors of the predictions made with the flight dynamics model of this paper relative to the respective flight test data, are also annotated in Fig. 9. The corresponding relative errors are shown both for the case that the aerodynamic influence of the fuselage is included in the analysis, as well for that where it is neglected. For the rotor power requirement P_{rotor} (Fig. 9(a)) the relative error for each advance ratio is normalised using the respective value of shaft power reported in the flight test data. For the rotor control angles θ_0, θ_{1s} and θ_{1c} (Figs 9(b), (c), and (d) respectively) error normalisation is carried out using the associated control range values θ^R for the Bo105 hingeless rotor system, where $\theta_0^R = 19{\cdot}6$, $\theta_{1s}^R = 15{\cdot}5$, and $\theta_{1c}^R = 10$. As regards the fuselage attitude angle Θ (Fig. 9(e)) error normalisation is performed using the range of Θ from $\bar{\mu} = 0$ to $\bar{\mu} \approx 0{\cdot}36$ as predicted by the flight dynamics model of this paper $|\Theta(\mu = 0{\cdot}36) - \Theta(\mu = 0)|$.

Figures 9(a) and (b) present trim values of main rotor power requirement P_{rotor} and collective pitch angle θ_0, respectively. Good correlation can be observed between flight test data and simulations carried out with the described flight dynamics model regarding both trim outputs. The relative error for power requirement P_{rotor} is approximately –3% near hover and varies between ±15% in forward flight with respect to both sets of numerical predictions. As regards the collective pitch angle θ_0, the relative error starts roughly at –3% in hover and rises up to –10% for $\bar{\mu} \approx 0{\cdot}24$. It is noted that for hovering flight, the estimated download due to impingement of the rotor wake on the fuselage reaches roughly 8% of the rotorcraft weight. This effectively needs to be compensated for by increasing the collective pitch angle in order to match the required rotor thrust.

The aforementioned deviations in power requirement and collective pitch angle at higher values of advance ratio are attributed to the underprediction of fuselage drag. This is suspected to be a deficiency in the employed look-up tables of Ref. 24. This was also observed and elaborated in Ref. 25 where the same data was used to estimate the aerodynamic behaviour of the Bo105 fuselage. Furthermore, good agreement is exhibited between predictions made with the present approach and the free-wake/FEA simulation model of Ref. 25 for $\bar{\mu} \geq 0{\cdot}15$. The correlation for θ_0 between the two models is excellent for $\bar{\mu} \geq 0{\cdot}15$, where the flow-field in the vicinity of the main rotor begins to be dominated by the free-stream flow. There is no noticeable difference in neither trim output between predictions made including the effect of the fuselage, and those without it.

The large deviations observed between the predictions reported in Ref. 25 and the respective flight test data with regards to P_{rotor} and θ_0 for $\bar{\mu} \leq 0{\cdot}1$, are attributed to the relatively crude representation of the wake geometry. The free-wake model used for the simulations carried out in Ref. 25 assumes that the wake geometry consists solely of the tip-vortex filaments produced by the rotor blades. As a result, the aerodynamic effect of the shear layer behind each blade is not taken into account. Furthermore, the circulation of each tip vortex filament that is instantaneously shed into the wake, is assumed to be equal to the bound circulation of the corresponding blade. This

https://doi.org/10.1017/S0001924000010563 Published online by Cambridge University Press

is done in order to satisfy Kelvin's theorem for the conservation of circulation. However, this approach effectively leads to excessively large, non-physical wake-induced velocities near the blade tips which serve to increase the collective pitch and rotor power requirement for a given thrust setting. This deficiency in rotor wake-modelling has been further elaborated in Ref. 25.

Figures 9(c) and (d) present trim variations of longitudinal (θ_{1s}) and lateral (θ_{1c}) cyclic pitch control input angles, respectively. It can be noticed from Fig. 9(c) that the presence of the fuselage affects only slightly the calculated values of θ_{1s}. As elaborated earlier, the induced velocity perturbation component $\bar{w}$ is predominantly responsible for influencing the rotor blade's incidence through the associated aerodynamic interference effects. Figures 4(a) and (b) show that the $\bar{w}$ perturbation distribution on the rotor disc is axisymmetric with respect to the longitudinal centreline ($Y = 0$m). Therefore, it is understood that no once-per-rev aerodynamic excitation is induced in a sinusoidal manner by the helicopter fuselage on the main rotor blades. However, during trimmed flight the rotor tip-path plane is tilted laterally in order to compensate for the rolling moments exerted by the tail-rotor. This essentially produces a small lateral bias of the fuselage induced velocity perturbations on the main rotor tip-path plane. Hence, a finite but small compensation is required in longitudinal cyclic θ_{1s} which tends to increase with flight speed as shown in Fig. 9(c).

Good agreement is observed between simulations carried with the present numerical approach and flight test data. The relative error for θ_{1s} is consistently between ±7% throughout the forward flight speed range. The relatively large deviation ($\approx -10\%$) observed for near-hover conditions ($\bar{\mu} \leq 0{\cdot}05$) is attributed to the impingement of the rotor wake on the horizontal stabiliser which leads to a large positive pitching moment. The obtained results suggest that the magnitude of this phenomenon is underpredicted by both flight dynamics simulation models.

Figure 9(d) shows that the estimated values of the lateral cyclic pitch control angle (θ_{1c}) are influenced considerably by the presence of the fuselage, especially at high-speed flight conditions. This is due to the fact that the distribution of the flow perturbation $\bar{w}$ induced by the fuselage is highly asymmetrical with respect to the lateral centreline of the rotor disc ($X \approx 0{\cdot}7$m). Therefore an effective once-per-rev harmonic excitation is exerted on the rotor blades in a cosinusoidal manner. These longitudinal inflow gradients of fuselage induced flow normal to the rotor disc (Fig. 5(b)) are essentially compensated by the control system by increasing θ_{1c}. This behaviour is more pronounced at high-speed flight, where the fuselage induced flow becomes significant. Figure 9(d) shows that for $\bar{\mu} \approx 0{\cdot}36$ the required increase in θ_{1c} when rotor-fuselage interaction effects are considered may be of the order of 5% of the total control range in lateral cyclic (10 for the Bo105 helicopter).

Good predictive qualities are exhibited by the described flight dynamics simulation model for $\bar{\mu} \geq 0{\cdot}1$. It can be observed that θ_{1c} is underpredicted for $\bar{\mu} \approx 0{\cdot}05$ with a relative error of the order of –10%. This is attributed to the rotor wake roll-up effect which is not accounted for by the Peters-He finite-state induced flow model. The roll-up of the blade tip vortices downstream of the main rotor leads to a large longitudinal inflow gradient at very low values of advance ratio. Thus, the control system compensates by increasing θ_{1c} in order to counter-act this longitudinal component of induced flow. It can be observed that the simulation model of Ref. 25 which incorporates a free-wake approach, has essentially captured the required increase of θ_{1c} for $\bar{\mu} \approx 0{\cdot}05$. The relative error between numerical predictions and flight test data is consistently within the range of ±3 for $\bar{\mu} \geq 0{\cdot}1$. Better correlation in terms of reduced error is observed between flight tests and simulations carried out with the inclusion of rotor-fuselage interaction effects. This is more pronounced at higher values of $\bar{\mu}$ where the fuselage induced flow becomes significant relative to the wake induced flow.

Figure 9(e) presents trim values for the fuselage pitch attitude angle Θ. It can be observed that

https://doi.org/10.1017/S0001924000010563 Published online by Cambridge University Press

the aerodynamic influence of the fuselage on the pitch attitude angle required for trim is negligible. Good agreement is noted between predictions made with the present real-time flight dynamics simulation model and the non-real-time high-complexity method of Ref. 25. Considerable scatter is observed in the available flight test data for $\bar{\mu} \leq 0{\cdot}1$. This is attributed to the unsteady influence of the rotor wake on the aerodynamic behaviour of the horizontal stabiliser in near-hovering flight, which makes it difficult to identify a representative pitch attitude angle for trim. Moreover, this effect is underpredicted by both helicopter flight dynamics models. As a result, the relative error between the numerical predictions and the flight test data oscillates notably within a range of ±20% throughout the flight speed range for which comparisons are presented.

3.3 Effects of fuselage aerodynamic interference on low-frequency helicopter dynamics

This section aims to present a first-order identification of the dominant effects of rotor-fuselage aerodynamic interaction on the estimated S & C derivatives for the low-frequency unsteady motion of the Bo105 helicopter. Analyses were carried out for straight and level flight at $V \approx 41{\cdot}15 \text{ms}^{-1}$ (80 knots) corresponding to an advance ratio of $\bar{\mu} \approx 0{\cdot}189$. The simulated flight altitude was roughly 914m (3,000ft). The obtained S & C derivatives were compared with their reciprocal values identified from flight test data in Ref. 56. Reference 56 reported on the application of system identification methods for the extraction of 6-DOF models in terms of S & C derivatives from flight test measurements. Results were obtained from various research establishments/working group members that include the U.S Army Aeroflightdynamics Directorate (AFDD), the German aerospace centre DLR (Deutsches Zentrum für Luft- und Raumfahrt), and the Canadian National Aeronautical Establishment (NAE – now National Research Council (NRC)).

Table 1 presents correlations for some of the most important S & C derivatives of the Bo105 helicopter, between predictions made with the described flight dynamics simulation model and the respective values identified from flight tests. Simulations were performed with the inclusion of fuselage induced velocity perturbations (Sim. (*wf*)) as well as without (Sim. (*nf*)). The percentage deviations of the estimated S & C derivatives that include the aerodynamic influence of the fuselage relative to those that do not, are also shown in Table 1 for consistency (Rel. dev.(%)). Comparisons are carried out with identification results reported by AFDD, DLR, and NAE. The respective standard deviations (σ) of the identified derivatives are provided in parentheses. These represent the theoretically lowest achievable standard deviation for each identified derivative (Cramer-Rao lower bounds). According to Ref. 56 these standard deviations are unrealistically small and it is recommended to multiply them by a factor of 5-10 in order to obtain more reasonable estimates.

It can be observed from the data presented in Table 1 that there are significant differences in the identified values for most of the derivatives of interest. Fairly accurate prediction of the direct force damping (X_u and Y_v) and heave damping (Z_w) derivatives is demonstrated, especially considering the differences noted in the identification results along with the respective standard deviations. Reference 56 attributed the larger values of Y_v identified by NAE and AFDD to a lateral speed measurement problem. The effect of the fuselage on the predicted values of the force and heave damping derivatives appears to be of the order of 1-3%. Thus, no appreciable improvement is observed in the obtained numerical results compared to the derivatives identified from flight tests.

Table 1 shows that the speed and incidence static stability derivatives, M_u and M_w, are quite under and overpredicted, respectively. For the given advance ratio ($\bar{\mu} \approx 0{\cdot}189$), these derivatives are influenced significantly by the contribution of the aerodynamic fuselage pitching moment. This component is modelled using the respective look-up tables provided in Ref. 24. Thus, any modelling uncertainties identified in the trim analysis section regarding the look-up tables of

https://doi.org/10.1017/S0001924000010563 Published online by Cambridge University Press

Table 1
Effects of fuselage induced flow on the estimated stability and control derivatives of the Bo105 helicopter – Comparison with system identification results from flight tests[56]

Derivative	unit	AFDD (σ)	DLR (σ)	NAE (σ)	Sim.(nf)	Sim.(wf)	Rel. dev.(%)
X_u	1/sec	–0·038 (0·0036)	–0·059 (0·0006)	–0·050 (0·0094)	–0·0301	–0·0309	2·657
Y_v	1/sec	–0·221 (0·011)	-0.170 (0·0030)	–0.279 (0·005)	–0·1084	–0·1095	1·014
Z_w	1/sec	–1·187 (0·0555)	–0·998 (0·0072)	–1·106 (0·013)	–0·9418	–0.9097	–3·408
M_u	rad/(m·sec)	–	0·029 (0·0004)	0·0078 (0·001)	0·0023	0·0072	213·043
M_w	rad/(m·sec)	0·096 (0·0064)	0·053 (0·0011)	0·0696 (0·0022)	0·1337	0·1487	11·219
L_v	rad/(m·sec)	–0·207 (0·021)	–0·271 (0·004)	–0·270 (0·0071)	–0·2563	–0·2776	8·310
L_w	rad/(m·sec)	0·168 (0·014)	0·116 (0·0035)	0·116 (0·007)	0·1234	0·1398	13·290
M_q	1/sec	–4·493 (0·235)	–3·496 (0·047)	–2·992 (0·074)	–4·3148	–4·2913	0·5446
L_p	1/sec	–8·779 (0·641)	–8·501 (0·011)	–7·048 (0·201)	–6·0726	–6·0918	–0·316
M_p	1/sec	–0·998 (0·066)	–0·419 (0.038)	–1·414 (0·066)	–0·9420	–0·9101	–3·386
L_q	1/sec	3·182 (0·624)	3·037 (0·125)	4·454 (0·222)	4·3013	3·9009	–9·308
N_r	1/sec	–1·070 (0·061)	–0·858 (0·0068)	–1·017 (0·0234)	–0·9438	–0·9423	–0·158
L_r	1/sec	0·991 (0·187)	0·410 (0·036)	0·434 (0·055)	0·1166	0·12937	10·951
N_p	1/sec	–0·466 (0·150)	–1·057 (0·025)	–0·692 (0·061)	–0·7651	–0·7673	0·261
$Z_{\theta 0}$	m/(sec^2·%)	–0·388 (0·02)	–0·349 (0·002)	-0·337 (0·005)	–0·3664	–0·3681	0·463
$M_{\theta 1s}$	m/(sec^2·%)	0·098 (0·0043)	0·093 (0·001)	0·0787 (0·0015)	0·0782	0·0781	0·139
$L_{\theta 1c}$	m/(sec^2·%)	0·179 (0·0139)	0·185 (0·0023)	0·1361 (0·0036)	0·0787	0·0786	–0·012
$M_{\theta 1c}$	m/(sec^2·%)	–	–0·009 (0·0008)	0·0106 (0·0013)	0·0110	0·0110	0·15
$L_{\theta 1s}$	m/(sec^2·%)	0·073 (0·0064)	0·024 (0·0025)	–0·005 (0·0044)	–0·0567	–0·0564	–0·529

Ref. 24, have effectively propagated to the numerical results presented in Table 1. It is important to notice the good correlation between simulation and identification for the respective rolling moment derivatives, L_v and L_w. The aforementioned modelling uncertainties have not affected the predicted values of L_v and L_w simply because the analysis assumes negligible aerodynamic fuselage rolling moment.

https://doi.org/10.1017/S0001924000010563 Published online by Cambridge University Press

The effects of rotor-fuselage aerodynamic interaction on the aforementioned derivatives are significant. Specifically, the estimated value for the speed stability derivative M_u almost triples when the aerodynamic interaction effects are accounted for, thus giving excellent agreement with the value identified by NAE. However, the agreement with the DLR data in terms of the value for M_u is still poor. Relative differences of the order of 8-13% are noted for the remaining moment derivatives when rotor-fuselage interaction effects are accounted for, with all derivatives tending to increase in terms of absolute values. A definitive conclusion cannot be reached on whether the predictions were improved with the inclusion of rotor-fuselage interaction effects (with the exception of M_u). This is due to the large discrepancies noted between the identified derivatives along with the corresponding standard deviations of the identification process. However, to a first-order only, the trend observed in the numerical results suggests that inclusion of aerodynamic interference effects may serve to improve the correlations with the stability derivatives identified from flight test data.

The pitch and roll damping derivatives, M_q and L_p respectively, are influenced by effects that are both dynamic as well as aerodynamic in nature. These are related to the gyroscopic precession of the blades due to the angular motion of the hub, as well as to the in-plane lift and drag forces generated by aerodynamic loads[58]. It can be observed that the described flight dynamics model has yielded pitch and roll damping derivatives that are in very good agreement with the ones identified by the working group members. The numerical predictions carried out suggest that the aerodynamic effect of the fuselage on the pitch and roll damping derivatives is of the order 0·5%. This effect can be considered negligible and can be traced back to the slightly different rotor trim state, as shown in Fig. 9, which is due to the inclusion of rotor-fuselage interference effects.

Accurate determination of the pitch-roll cross-coupling derivatives (M_p and L_q) from first-principles is an issue of great current interest to the helicopter flight dynamics community. The contributing factors are predominantly aerodynamic in nature and comprise linear as well as nonlinear components. The linear part is related to the first harmonic variation of blade incidence, generated by the pitch/roll angular motion of the shaft. The nonlinear part is significantly more complex and is related to the effective curvature of the wake during pitching or rolling motion. The Zhao-Prasad wake distortion model which caters for the effect of wake curvature, has been utilised for the predictions reported in this paper. The effectiveness of this approach is evident from the fact that the estimated values for the pitch-roll cross coupling derivatives (M_p and L_q) lie within the range of the corresponding system identification results reported in Ref. 56.

It can be observed that the presence of the fuselage affects predominantly the cross-coupling derivative L_q that is associated with the pitching motion of the aircraft, whilst M_p changes only slightly. This behaviour is attributed to the somewhat axisymmetric geometry of the fuselage which does not induce significant velocity perturbations when rotating about the roll axis. However, for pitching motion about the aircraft CG, the fuselage induces a considerable longitudinal inflow gradient at the rotor tip-path plane, whose features resemble closely the flow-field illustrated in Fig. 5(b). This inflow gradient essentially translates to 1P harmonic forcing that is exerted on the blades in a cosinusoidal manner (Cos ψ_i, (t), $i = 1, \ldots N_b$). However, because of the approximately 90 degree phase lag, the blades respond sinusoidally (Sinψ_i, (t), $i = 1, \ldots N_b$), thus generating off-axis hub moments that contribute to the total rolling moment L that is exerted on the aircraft.

It can be observed that the yaw-damping derivative N_r was also accurately estimated by the described flight dynamics simulation model. Good correlation can also be noticed between analysis and identification results considering the roll-yaw cross-coupling derivative N_p. However, L_r appears to be quite underestimated when compared to the respective identification results. However, it is emphasised that large standard deviations are reported by all working group members for the specific derivative, thus indicating that it was identified poorly. The presence of the fuselage seems

to have a negligible effect on N_r and N_p. However, the predicted value of L_r was increased by almost 11%, relative to the case that the fuselage effects are omitted. A definitive conclusion on whether the inclusion of the fuselage has improved the nonlinear predictions cannot be reached due to the fact that L_r was identified poorly by the various working group members.

The control derivatives in Table 1 are given as fractions of the respective control displacements, with 100% of displacement corresponding to full control travel[56]. It can be observed that the influence of the fuselage in the obtained control derivatives is consistently below 1%. This deviation is attributed predominantly to the effective change in the helicopter trim state as shown in Fig. 9 for $\bar{\mu} \approx 0{\cdot}189$. It is noted that the effect of wake impingement on the fuselage for the specific set of flight conditions can be considered negligible. This is because of the relatively large wake skew angle combined with a low wake induced flow. For these conditions the rotor wake impinges on only a small area of the aft portion of the fuselage. As such, the effective impingement of the rotor wake on the aircraft does not serve to alter the induced flow perturbations considerably. Thus, no further influence of the fuselage is expected in the analytically estimated control derivatives.

Good agreement can be noted between analytical predictions and system identification results. for the thrust derivative Z_{θ_0}. It can also be observed that the on-axis longitudinal cyclic control derivative ($M_{\theta_{1s}}$) was fairly well captured. However, the derivative for on-axis lateral cyclic control ($L_{\theta_{1c}}$) appears to be quite underpredicted compared to the identified values. Reference 56 elaborated on the sensitivity of the identified control derivatives to the selection of equivalent time-delays for the actuator and rotor dynamics. The control derivatives were identified assuming a single time-delay for each control input. However, the present approach extracts the perturbation forces and moments when quasi-steady periodic conditions are obtained. Hence, different time-delays are assumed in the identified derivatives yielded by the various group members and also in the process of analytical derivation. This leads to exacerbated deviations between the identified values themselves, as well as compared to the predictions. Reference 56 presented further identification results from other working group members that yielded values for $L_{\theta_{1c}}$ that are very close to those estimated.

Even larger differences are observed considering the identified off-axis control derivatives $M_{\theta_{1c}}$ and $L_{\theta_{1s}}$. It is worth noticing that derivatives of different sign are identified by certain group members. This indicates a difficulty in identifying the off-axis control derivatives. It is noted that the predicted value of $M_{\theta_{1c}}$ agrees well in terms of both magnitude and sign with the corresponding value identified by NAE. As regards $L_{\theta_{1s}}$, although it is in agreement with the value identified by NAE in terms of sign, it is considerably larger in terms of magnitude. This is also attributed to the dependence of the identified control derivatives on the selection of equivalent time-delays.

3.4 Effects of fuselage aerodynamic interference on oscillatory structural blade loads

Figures 10-15 present correlations between nonlinear predictions made with the described aeroelastic rotor model and flight test measurements of oscillatory structural blade loads, for the full-scale hingeless rotor of the Bo105 helicopter. The presented flight test data were extracted from Ref. 54. Simulations were carried out with the inclusion of rotor-fuselage aerodynamic interaction effects (Sim. (*wf*)) as well as without (Sim. (*wf*)). Results are shown for straight and level flight corresponding to two different advance ratios; $\bar{\mu} = 0{\cdot}197$ and $\bar{\mu} = 0{\cdot}306$. The respective rotor shaft angles relative to the free-stream flow are; $\alpha_s = -4{\cdot}0°$ and α_s $-7{\cdot}7°$, respectively. In order to maintain consistency with the available flight test data from Ref. 54, comparisons of flapwise and chordwise bending moment are shown for different mid-span radial locations. Flapwise bending

https://doi.org/10.1017/S0001924000010563 Published online by Cambridge University Press

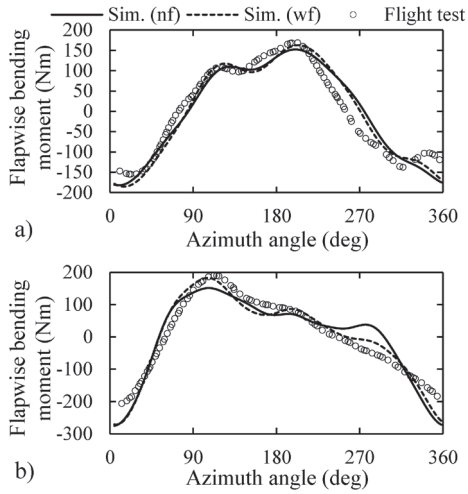

Figure 10. Effect of fuselage induced flow perturbations on the predicted oscillatory flapwise blade bending moment for r/R = 0·144 - Comparison with flight test data extracted from Ref. 54: (a) $\bar{\mu}$ = 0·197, α_s = –4·0°, (b) $\bar{\mu}$ = 0·306, α_s = –7·7°.

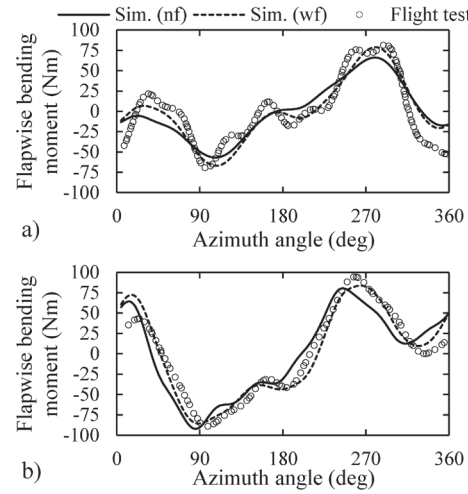

Figure 11. Effect of fuselage induced flow perturbations on the predicted oscillatory flapwise blade bending moment for r/R = 0·57 - Comparison with flight test data extracted from Ref. 54: $\bar{\mu}$ = 0·197°, α_s = –4·0°, (b) $\bar{\mu}$ = 0·306, α_s = –7·7°.

moment results at mid-span correspond to r/R = 0·57, while the respective chordwise bending moments are presented for r/R = 0·45. Both flap and chord bending moment predictions at the hub are extracted for r/R = 1·44. Torsional moment predictions are presented for a single radial location corresponding to r/R = 0·40, due to lack of available flight test data.

Figures 10 and 11 present correlations of oscillatory flapwise blade bending moment between predictions made with the described aeroelastic rotor model and flight test measurements. Results are presented for the effective blade root (r/R = 0·144) and near mid-span (r/R = 0·57) radial stations in Figs 10 and 11, respectively.

Good agreement is exhibited between nonlinear predictions and flight test measurements with regards to the oscillatory component of flapwise loading at the effective blade root location (Fig. 10) for both values of advance ratio. The 1P loading component was accurately captured in terms of both amplitude and phase, considering both sets of nonlinear simulations. This is due to the fact that rotor trim was performed for prescribed thrust and hub moment settings. The comparisons suggest that the 2P and 3P oscillatory components of flap bending moment are slightly over and underpredicted, respectively. Inclusion of rotor-fuselage aerodynamic interaction results in slightly improved estimation of 3P and 2P oscillatory loading for $\bar{\mu} = 0{\cdot}197$ and $\bar{\mu} = 0{\cdot}307$, in that order.

Good correlation of oscillatory flap moment between nonlinear simulations and flight test measurements can also be observed for the near mid-span blade location (r/R = 0·57) in Fig. 11. The 1P component of flapwise loading was fairly accurately captured for both values of advance ratio. Good agreement is also noted with respect to the 2P and 3P components of oscillatory flapwise bending moment, considering both sets of nonlinear predictions. Once again it can be noticed that inclusion of rotor-fuselage interaction serves to improve the predictive qualities considering the amplitude of the 3P oscillatory component of flapwise loading. The higher frequency 8P harmonic content observed in the flight test data for $\bar{\mu}$ = 0·197 is attributed to the fourth flap mode of the blade since its natural frequency is also very close to 8P. This harmonic component as not captured

https://doi.org/10.1017/S0001924000010563 Published online by Cambridge University Press

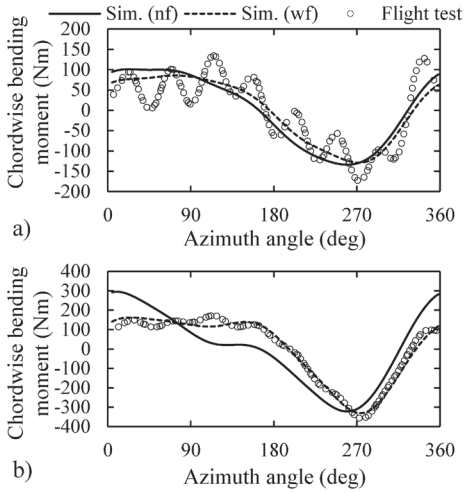

Figure 12. Effect of fuselage induced flow perturbations on the predicted oscillatory chordwise blade bending moment for r/R = 0·144 - Comparison with flight test data extracted from Ref. 54: (a) $\bar{\mu}$ = 0·197, α_s = –4·0°, (b) $\bar{\mu}$ = 0·306, α_s = –7·7°.

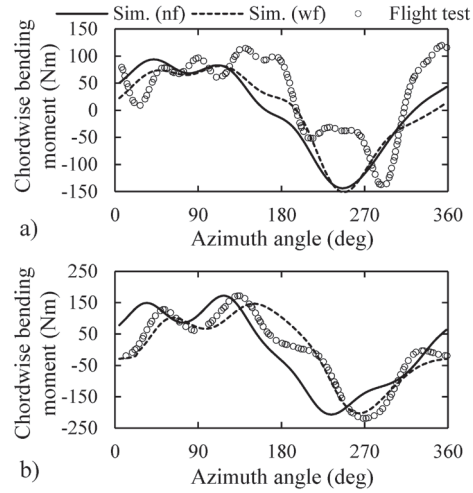

Figure 13. Effect of fuselage induced flow perturbations on the predicted oscillatory chordwise blade bending moment for r/R = 0·45 - Comparison with flight test data extracted from Ref. 54: (a) $\bar{\mu}$ = 0·197, α_s = –4·0°, (b) $\bar{\mu}$ = 0·306, α_s = –7·7°.

by the present modelling approach despite the fact that associated modal content was included in the analysis, not even with the inclusion of the associated rotor-fuselage interference effects. This is attributed to the inherent difficulty of the employed blade element aerodynamics approach to predict the higher-frequency harmonic components (8P) of aerodynamic loading.

Figures 12 and 13 present correlations of oscillatory chordwise blade bending moment, between predictions made with the present aeroelastic rotor formulation and flight test measurements. Results are presented for the effective blade root (r/R = 0·144) and near mid-span (r/R = 0·45) radial stations in Figs 12 and 13, respectively.

Figure 12 shows that the basic waveform shape of chordwise bending moment at the blade root (r/R = 0·144) was adequately captured for both values of advance ratio. The comparisons carried out for $\bar{\mu}$ = 0·197 suggest that the predicted behaviour of the 1P component of chordwise loading is notably improved in terms of both amplitude and phase angle, when rotor-fuselage interaction effects are included in the analysis. However, both the 2P and 3P oscillatory components of chordwise loading are considerably underpredicted in terms of amplitude, even with the inclusion of the associated interference effects. Considering the case of $\bar{\mu}$ = 0·306, a significant improvement can be noted in the predicted behaviour of chordwise bending moment, reaching up to the third harmonic component of oscillatory loading (3P), when the effect of the fuselage is catered for. This is attributed to the increasing magnitude of the velocity perturbations induced by the fuselage at high-speed flight, relative to the wake-induced flow. The aerodynamic effect of the fuselage becomes more prominent at higher values of advance ratio due to the fact that the vortical wake is quickly swept away downstream by the free-stream flow.

It can be observed that higher-order harmonic content reaching up to 8P is present in the flight test measurements. This high-frequency content tends to decrease with increasing advance ratio and was not captured by the analysis. The 8P component of oscillatory chordwise loading observed in the flight test data is potentially attributed the effect of elastic flap/lag coupling that is present

https://doi.org/10.1017/S0001924000010563 Published online by Cambridge University Press

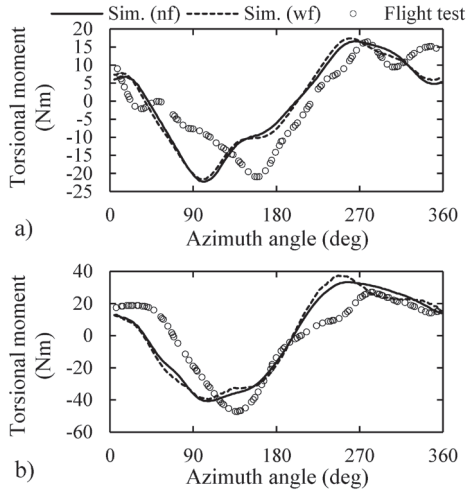

Figure 14. Effect of fuselage induced flow perturbations on the predicted oscillatory torsional blade moment for r/R = 0·40 - Comparison with flight test data extracted from Ref. 54: (a) $\bar{\mu}$ = 0·197, α_s = –4·0°, (b) $\bar{\mu}$ = 0·306, α_s = –7·7°.

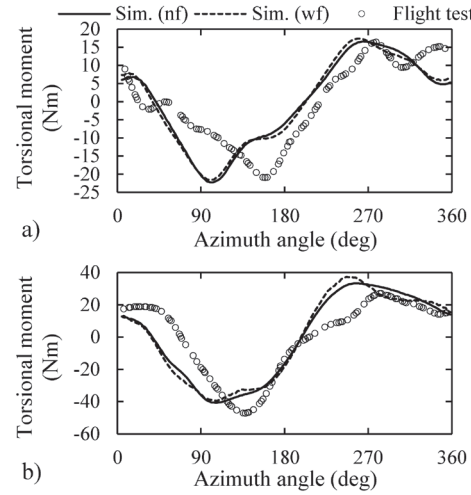

Figure 15. Effect of fuselage induced flow on the predicted vibratory flapwise bending moment for r/R = 0·144 - Comparison with flight test data extracted from Ref. 54: (a) $\bar{\mu}$ = 0·197, α_s = –4·0°, (b) $\bar{\mu}$ = 0·306, α_s = –7·7°.

in the fourth natural flap mode[29]. It is believed that, the 8P component of oscillatory chordwise loading observed in Fig 12(a) is directly related to the 8P flapwise loading component that was also noted in Fig 11(a). This effect has not been captured due to the aforementioned difficulty of the employed modelling approach to capture the high-frequency components of aerodynamic loading and also possibly because of the absence of elastic coupling in the employed modal content[29].

With respect to the radial location corresponding to r/R = 0·45, Fig. 13 demonstrates good agreement between nonlinear predictions and flight test measurements considering the 1P component of oscillatory chordwise loading. As regards the correlations carried out for $\bar{\mu}$ = 0·197, the predicted behaviour of the 3P harmonic component of oscillatory loading is considerably improved when the effect of the fuselage is included in the analysis. Once again it can be observed that high-frequency content resides in the flight test data that reaches up to the eighth harmonic of oscillatory loading (8P). This harmonic content was not captured by the proposed numerical approach, not even with the inclusion of rotor-fuselage aerodynamic interaction effects. Considering the case of $\bar{\mu}$ = 0·306, a significant improvement can be noted in the predicted behaviour of chordwise bending moment regarding predominantly the third harmonic (3P) of oscillatory loading, when the effect of the fuselage is included in the analysis. This is attributed to the large magnitude of the velocity perturbations induced by the fuselage at high-speed flight conditions.

Figure 14 presents correlations of oscillatory torsional blade moment for r/R = 0·40, between nonlinear predictions and flight test measurements. Good agreement can generally be observed for both values of advance ratio. It can be noticed that torsional moment at the particular radial location comprises predominantly 1P harmonic content. This content was adequately captured in terms of amplitude. However, there is an underprediction in the phase angle of 1P loading which reaches approximately 60º. This effectively leads to the appearance of peak loads at lower azimuth angles when compared to the measured data. Reference 54 mentioned that the Bo105 helicopter rotor that was deployed for the flight test measurements, essentially employed a different value of

https://doi.org/10.1017/S0001924000010563 Published online by Cambridge University Press

torsional stiffness for the pitch control system, in relation to the rotor configuration described in Ref. 53. This difference in torsional stiffness may have affected the blade's natural frequencies for torsional vibration[29], leading to different phase angles in the dynamic torsion response. Inclusion of rotor-fuselage interference effects does not result in improved predictions of torsional vibration, regarding neither set of flight conditions. Finally, it can be observed that higher harmonic content (2P and 3P) is of relatively low amplitude for $\bar{\mu} = 0{\cdot}197$ but increases substantially for $\bar{\mu} = 0{\cdot}306$.

Figure 15 presents a comparison between predictions and flight test measurements of the vibratory components of flapwise bending moment at the effective blade root location ($r/R = 0{\cdot}144$). A harmonic analysis was carried out on the measured and predicted waveforms of oscillatory flap loading at the blade root. Only the harmonic components capable of transmitting vibratory loads to the fuselage were retained. According to Ref. 59, for perfectly matched blades, the condition for retaining the kth harmonic of oscillatory flap moment in the calculated vibratory flap loading waveform can be expressed as: $k = m{\cdot}N_b\ 1$, $m = 1,2,3\ \ldots$. The harmonics not complying with this condition were essentially discarded from the reconstructed waveforms.

Figure 15 shows that the measured vibratory flap moment comprises predominantly 3P and 5P oscillatory loading that was adequately captured by the numerical approach described in this paper. Regarding the case of $\bar{\mu} = 0{\cdot}197$, inclusion of rotor-fuselage interference effects results in notably improved predictions considering the amplitude of the 3P component of flap bending moment. This effectively leads to better overall predictive qualities in terms of rotor induced vibration. For $\bar{\mu} = 0{\cdot}306$, including the effect of the fuselage does not result in better amplitude predictions for the 3P harmonic component, although a notable improvement can be observed in the respective phase angle. Although the amplitude of the 5P loading component was adequately captured for both advance ratios, the phase angle correlation with the flight test data is poor, even when the effect of the fuselage is included in the analysis. Finally, the simulations predicted gradually decreasing amplitude for the 5P harmonic component of flapwise loading with increasing advance ratio.

Although not included in this paper, a comparative evaluation was carried out to determine the effect of number of flow-states on the predicted oscillatory blade loads. Simulations were performed with 15, 33, 47, and 96 flow-states. The respective inflow models employed aerodynamic terms reaching up to the third, fourth, sixth, and eighth harmonic of oscillatory loading, respectively. It was found that the predicted loading waveforms converge after the inclusion of only 33 flow-states. The 8P harmonic content found in the measured data was not captured, not even with the inclusion of 96 flow-states. Hence, since the rotor model described in this paper focuses on harmonic content with frequency up to 4P, a total of 33 flow-states is considered to be sufficient in order to capture the aeroelastic behaviour of the rotor blades.

3.5 Effects of fuselage aerodynamic interference on nonlinear control response characteristics

This section aims to present a first-order investigation considering the effects of rotor-fuselage aerodynamic interaction on the nonlinear control response characteristics of the Bo105 helicopter. The obtained predictions are compared with flight test data reported in Ref. 57, as well as with results from simulations carried out in Ref. 25 (Free-wake/FEA) using a high-complexity, non-real-time flight dynamics simulation code.

It is noted that the simulation methodology of Ref. 25 utilises elastically and inertially coupled modal properties obtained from nonlinear FEA. A relaxation-type free-wake inflow model is deployed[60] which accounts for the effect of wake curvature due to maneuvering flight as well as for the self-induced roll-up of the tip vortices downstream of the main rotor. The present numerical approach does not account for elastic coupling in the employed modal properties. However, inertial

https://doi.org/10.1017/S0001924000010563 Published online by Cambridge University Press

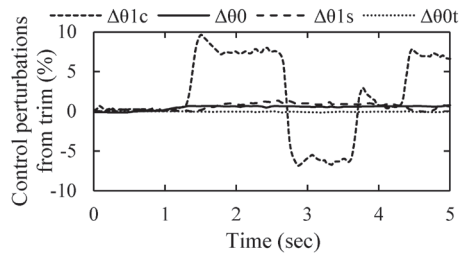

Figure 16. Control perturbations from trim for the selected near-hover manoeuver; $\bar{\mu} \approx 0{\cdot}040$.

coupling is thoroughly retained through proper inclusion of the corresponding forcing terms in the kinematic equations of elastic blade motion. The proposed approach caters for wake curvature effects due to manoeuvering flight, through augmenting the employed Peters-He finite-state inflow model[35,36] with the dynamic wake distortion model developed by Zhao-Prasad in Refs 46 and 47. However, the self-induced roll-up of the wake is not accounted for in the combined inflow formulation.

A representative manoeuver was selected to be simulated at near-hover flight conditions ($\bar{\mu} \approx 0{\cdot}040$). Figure 16 presents the time variations of the control deflections from trim as percentages of full control travel. The respective control schedule comprises predominantly deflections in lateral cyclic θ_{1c} which closely resembles a doublet control input. The specific maneuver is essentially part of a larger series of flight tests conducted for system identification purposes, as described in Ref. 57.

Figure 17 demonstrates the effect of fuselage induced flow on the predicted nonlinear response of the Bo105 helicopter to the selected control schedule for $\bar{\mu} \approx 0{\cdot}040$). Results are presented for the fuselage roll (on-axis response) and pitch rates (off-axis response) in Figs 17(a) and (b) respectively. Very good correlation in terms of both amplitude and phase can be observed in Fig. 17(a) between nonlinear predictions and flight test measurements, considering the on-axis response of the fuselage (roll rate p). Excellent agreement is also demonstrated between the present modelling approach and the high-complexity flight dynamics simulation code of Ref. 25. It can be noticed that the effect of fuselage induced flow on the predicted on-axis response is almost negligible for the specific advance ratio ($\bar{\mu} \approx 0{\cdot}040$). No notable difference is observed in the roll rate predictions when the associated aerodynamic terms are included in the nonlinear control response analysis.

Figure 17(b) shows that the proposed modelling approach was also successful in predicting the off-axis response of the fuselage (pitch rate q) with reasonable accuracy. Good correlation can be observed between flight test measurements and nonlinear predictions carried out both with and without the inclusion of the velocity perturbations induced by the fuselage. Good agreement can also be noted between the present real-time simulation model and the non-real-time flight dynamics code of Ref. 25. Once again, it can be noticed that inclusion of rotor-fuselage aerodynamic interference effects has not resulted in improved off-axis response predictions.

The aerodynamic effect of the fuselage on the control response of the Bo105 helicopter was found to be small due to the fact that the selected control manoeuvre is executed at low-speed flight ($\bar{\mu} \approx 0{\cdot}040$). Hence, any induced velocity perturbations arise due to the impingement of a cylindrical representation of the rotor wake on the fuselage, as well as due to its respective angular motions (roll, pitch and yaw). It is evident from the results presented in Fig. 17 that these effects are relatively small and can be safely neglected in a nonlinear control response analysis at near-hovering flight.

https://doi.org/10.1017/S0001924000010563 Published online by Cambridge University Press

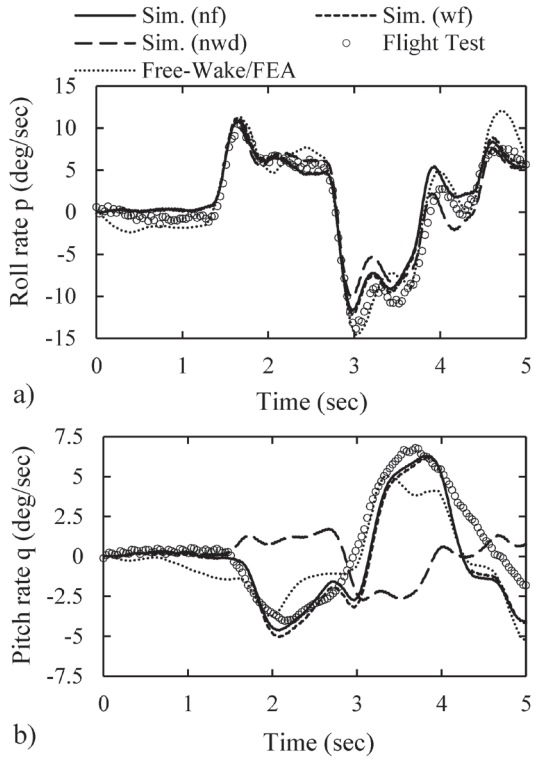

Figure 17. Effect of fuselage induced flow on the predicted response of the Bo 105 helicopter for the selected control manoeuver, $\bar{\mu} \approx 0{\cdot}040$: a) Fuselage roll rate (on-axis response), (b) Fuselage pitch rate (off-axis response).

Figure 17 also shows that with regards to the first second of flight simulation where the control deflections from trim are minimum, the respective roll and pitch rates are practically zero. This indicates that the developed trim procedure was successful in obtaining a trim state that is fully compatible with nonlinear control response simulation. This observation confirms the validity of the numerical approach employed for obtaining rotor trim. However, this is not the case considering the flight dynamics code of Ref. 25 where substantial deviations from trim are observed with respect to the first second of simulation. This was previously attributed to a deficiency of the incorporated numerical approach for finding rotor trim and was further elaborated in Ref. 25.

The significance of including dynamic wake distortion effects when it comes to accurate prediction of fuselage off-axis response (pitch rate q) is also evident from the results presented in Fig. 17(b). Considering the simulations conducted excluding the aforementioned effects (Sim. (*nwd*)), the predicted off-axis response correlates poorly with flight test data. This observation is in agreement with typical trends reported by other investigators[46,47]. A small improvement in the on-axis response can also be observed in Fig. 17(a) when accounting for wake distortion. This is attributed to the strong cross-coupling characteristics of the Bo105 helicopter. It is believed that improvement of the off-axis response has inevitably affected the predicted on-axis behaviour in a favorable manner due the substantial cross-coupling involved[56].

https://doi.org/10.1017/S0001924000010563 Published online by Cambridge University Press

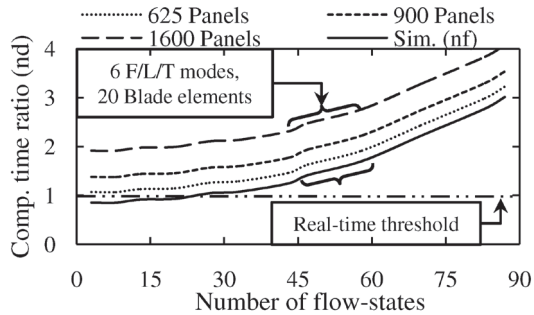

Figure 18. Influence of number of flow-states and number of panels on the computational time ratio for a personal computer equipped with a 2·3GHz CPU and 4GB of RAM.

3.6 Assessment of computational time requirements and method applicability in real-time

In order to evaluate the suitability of the proposed numerical approach for real-time simulation, the computational time requirements associated with nonlinear control response analysis were thoroughly assessed. An effective parameter was defined, namely the computational time ratio, as the computational time required per transient control response simulation time. Thus, a value of computational time ratio less that unity (real-time threshold) essentially allows for the nonlinear flight dynamics simulation model to be deployed in real-time.

Figure 18 showcases the effect of number of panels used for the numerical discretisation of the fuselage geometry, along with the number of employed flow-states, on the computational time ratio. Time measurements were conducted on a personal computer equipped with 4 gigabytes (GB) of random access memory (RAM) and a dual-core central processing unit (CPU) operating at 2·3 gigahertz (GHz). A total of 20 elements were used for the aerodynamic discretisation of each blade. Six flap-lag-torsion modes were incorporated for the structural representation of the elastic blades. A time-step of $\Delta t = 2{\cdot}10^{-3}$sec was employed for time-marching leading to an azimuth-step of 5°.

It can be noticed that the effect of number of panels on the computational time ratio is significant. Computational times change considerably with the employment of up to 1,600 quadrilateral planar panels for the discretisation of the fuselage geometry. However, a sensitivity analysis conducted by the author suggests that no noticeable change occurs in the predicted flow perturbations (Figs. 5-8) when the number of panels is increased beyond 700. The influence of number of flow-states is considered moderate if one accounts for the fact that computational time almost triples when increasing the number of flow-states by a factor of thirty. It is noted that a number of 33-45 flow-states was found to be sufficient for typical aeroelasticity applications[28-30]. However, further aerodynamic refinement is essential when higher-harmonic loading is required in the analysis.

Figure 18 demonstrates that for the relatively low-end machine used in this work, nonlinear flight simulation can be achieved in near-real-time with a computational time ratio of approximately 1·2, using up to 33 flow-states and 625 panel elements. This results in an aeroelastic rotor-fuselage model of sufficient fidelity for nonlinear control response analysis including the effects of rotor-fuselage aerodynamic interaction. The developed approach is expected to run significantly faster on high-end machines used routinely in industry and academia, thus allowing real-time simulation using model configurations of substantially higher fidelity. Thus, it can be concluded that the proposed approach is capable of implementation and execution in real-time flight dynamics applications.

https://doi.org/10.1017/S0001924000010563 Published online by Cambridge University Press

4.0 CONCLUSIONS

An integrated framework targeting the simulation of rotor-fuselage aerodynamic interaction effects in real-time helicopter flight dynamics applications, has been described. A mathematical formulation was employed for the treatment of elastic blade kinematics in the time-domain. The developed method was coupled with a finite-state induced flow model, an unsteady blade element aerodynamics model, and a dynamic wake distortion model. A three-dimensional, steady-state, potential flow source-panel method was employed for the prediction of induced flow in the vicinity of the fuselage due to its presence in the free-stream and within the rotor wake. The combined aeroelastic rotor-fuselage model was implemented in a flight dynamics simulation code. The integrated methodology was deployed in order to investigate the effects of rotor-fuselage aerodynamic interaction on trim performance, stability and control derivatives, oscillatory blade loads, and nonlinear control response for a hingeless rotor helicopter modelled after the Eurocopter Bo105.

The general conclusions arising from the completion of this work can be summarised as follows:

1. Good agreement was found between potential flow predictions and experimental measurements for an isolated fuselage, considering the induced velocity perturbations at the imaginary rotor tip-path plane. Larger deviations were observed in the vicinity close to the rotor hub which were attributed to the absence of the rotor shaft and hub components in the modelled geometry.
2.. The developed modelling method exhibited accurate predictive qualities with regards to trim control angles for straight and level flight. It was shown that the laterally asymmetrical distribution of fuselage induced flow results in a once-per-rev cosinusoidal forcing on the rotor blades. This harmonic forcing needs to be counteracted by the control system through increasing the lateral cyclic pitch angle θ_{1c}. The required increase for $\bar{\mu} \approx 0{\cdot}36$ is of the order of 5% of the total control range in lateral cyclic, considering the case of the Bo105 helicopter.
3. The proposed modelling approach was successful in obtaining reasonably accurate estimates of stability and control derivatives. The speed and incidence static stability derivatives (M_u and M_w) were found to be substantially influenced by rotor-fuselage aerodynamic interaction effects. The predicted pitch and roll damping derivatives (M_q and L_p) were essentially not affected by the presence of the fuselage. However, the pitch-roll cross-coupling derivative L_q was found to be considerably influenced by the associated interference effects. This was attributed to the laterally asymmetrical flow-field that is induced by the fuselage during pitching motion.
4. Predictions of structural blade loads were found to be accurate in terms of amplitude and phase up to the third harmonic component of oscillatory loading. The model was unable to capture the higher frequency components (8P) residing in the measured loading waveforms.
5. A significant improvement was noted in the predicted behaviour of chordwise bending moment for $\bar{\mu} \approx 0{\cdot}306$ when the effect of the fuselage was included in the analysis. This was attributed to the increased magnitude of the fuselage induced velocity perturbations at high-speed flight, relative to the wake-induced flow. Inclusion of rotor-fuselage interaction effects also resulted in improved amplitude predictions considering the 3P component of oscillatory flapwise loading. No improvement was observed with respect to the prediction of oscillatory torsional moment.
6. The developed flight dynamics simulation model was able to predict the on-axis as well as off-axis response of the Bo105 helicopter to pilot control inputs for a representative pitch/roll manoeuver at near-hover conditions. The aerodynamic effect of the fuselage was found to be small at low-speed flight and can be safely neglected in a pitch/roll control response analysis for similar flight conditions.

https://doi.org/10.1017/S0001924000010563 Published online by Cambridge University Press

7. The described approach is suitable for near-real-time flight dynamics applications including the effects of rotor-fuselage aerodynamic interaction on a relatively low-end personal computer. Simulations can be carried out with sufficient fidelity for nonlinear control response analysis with simultaneous prediction of oscillatory structural blade loads.

Hence, the mathematical formulation described in this paper enables the implementation of rotor-fuselage aerodynamic interaction effects in real-time helicopter flight dynamics applications, without resorting to computationally expensive, high-complexity modelling methods. It is compatible with every rotor inflow and blade element aerodynamics theory that can operate in the time-domain. The proposed approach is readily available for implementation in existing flight dynamics simulation codes that utilise the standard fuselage axes system, without any change in the offered expressions.

ACKNOWLEDGEMENTS

The author would like to kindly acknowledge Dr Vassilios Pachidis, Dr David MacManus, and Professor Pericles Pilidis from the Centre for Propulsion of Cranfield University, for their insightful advice and continuing support. Many thanks are also due to Mr Jos Stevens (NLR) and Mrs Christine Smith (AgustaWestland) for the numerous discussions on helicopter flight dynamics and performance.

REFERENCES

1. LEISHMAN, J., BHAGWAT, M. and BAGAI, A. Free-vortex filament methods for the analysis of helicopter rotor wakes, *J Aircr*, September-October 2002, **39**, (5), pp 759-775.
2.. BROWN, R.E. Rotor wake modeling for flight dynamic simulation of helicopters, *AIAA J*, January 2000, **38**, (1), pp 57-63.
3. RENAUD, T., O'BRIEN, D., SMITH, M. and POTSDAM, M. Evaluation of isolated fuselage and rotor-fuselage interaction using computational fluid dynamics, *J American Helicopter Soc*, January 2008, **53**, (1), pp 3-17.
4. BERRY, J. and BETTSCHART, N. Rotor-fuselage interaction: Analysis and validation with experiment, May 1997, NASA, TM 112859.
5. BERRY, J.D. and ALTHOFF, S.L. Computing induced velocity perturbations due to a helicopter fuselage in a free stream, 1989, NASA, TM-4113.
6. CRIMI, P. and TRENKA, A.R. Theoretical prediction of the flow in the wake of a helicopter rotor. Addendum: Effects due to a fuselage in a constant, nonuniform flow, 1966, Cornell Aeronautical Laboratory, BB-1994-S-3.
7. KEYS, C. Rotary-wing aerodynamics, Volume II - Performance prediction of helicopters, 1979, NASA, CR-3083.
8. JOHNSON, W. and YAMAUCHI, G.K. Applications of an analysis of axisymmetric body effects on rotor performance and loads, August 1984, Tenth European Rotorcraft Forum, The Hague, The Netherlands.
9. SCHWEITZER, S. Computational Simulation of Flow around Helicopter Fuselages, MSc thesis, 1999, Pennsylvania State University, USA.
10. GHEE, T., BERRY, J., ZORI, L. and ELLIOT, J. Wake geometry measurements and analytical calculations on a small-scale rotor model, 1997, NASA, TP 3584.
11. LORBER, P.F. and EGOLF, T.A. An unsteady helicopter rotor-fuselage interaction analysis, 1988, NASA, CR-4178.
12. LEE, B.S., JUNG, M.S. and KWON, O.J. Numerical simulation of rotor-fuselage aerodynamic interaction using an unstructured overset mesh technique, *J Aeronautical and Space Sci*, March 2010, **11**, (1), pp 1-9.
13. KELLY, M.E., DURAISAMY, K. and BROWN, R.E. Predicting blade vortex interaction, airloads and acoustics using the vorticity transport model, 23-25 January 2008, AHS Specialists' Conference on Aeromechanics, San Francisco, CA, USA.
14. VAN DER WALL, B.G. A comprehensive rotary-wing database for code validation: HART II International Workshop, *Aeronaut J*, February 2011, **115**, (1164), pp 91-102.

15. O'BRIEN, D.M. Analysis of Computational Modeling Techniques for Complete Rotorcraft Configurations, PhD thesis, May 2006, School of Aerospace Engineering, Georgia Institute of Technology, Atlanta, GA, USA.
16. O'BRIEN, D. and SMITH, M.J. Understanding the physical implications of approximate rotor methods using an unstructured CFD method, September 2005, 31st European Rotorcraft Forum, Florence, Italy.
17. O'BRIEN, D.M. and SMITH, M.J. Analysis of rotor-fuselage interactions using various rotor models, January 2005, AIAA 43rd Aerospace Sciences Meeting, No AIAA-2005-468, Reno, NV, USA.
18. BIEDRON, R.T. and LEE-RAUSCH, E.M. Computation of UH-60A airloads using CFD/CSD coupling on unstructured meshes, 3-5 May 2011, 67th Annual Forum of the Annual Forum of the American Helicopter Society, Virginia Beach, VA, USA.
19. JOHNSON, W. Technology drivers in the development of CAMRAD II, January 1994, American Helicopter Society Aeromechanics Specialists' Conference, San Fransisco, CA, USA.
20. BOYD, D.D. HART-II acoustic predictions using a coupled CFD/CSD method, 27-29 May 2009, 65th Annual Forum of the American Helicopter Society, Grapevine, TX, USA.
21. SA, J.H., YOU, Y.H., PARK, J.-S., JUNG, S.N., PARK, S.H. and YU, Y.H. Assessment of CFD/CSD coupled aeroelastic analysis solution for HART II rotor incorporating fuselage effects, 3-5 May 2011, 67th Annual Forum of the American Helicopter Society, Virginia Beach, VA, USA.
22. SMITH, M.J., LIM, J.W., VAN DER WALL, B.G., BAEDER, J.D., BIEDRON, R.T., BOYD, D.D., JAYARAMAN, B., JUNG, S.N. and MIN, B.-Y. The HART II International Workshop: An assessment of the state of the art in CFD/CSD prediction, *CEAS Aeronaut J*, December 2013, **4**, (4), pp 345-372.
23. VAN DER WALL, B.G., BAUKNECHT, A., JUNG, S.N. and YOU, Y.H. Semi-empirical modeling of fuselage-rotor interference for comprehensive codes: The fundamental model, *CEAS Aeronaut J*, May 2014, **5**, (2), pp 1-15.
24. PADFIELD, G.D. *Helicopter Flight Dynamics*, 2007, Blackwell Publishing, Oxford, UK.
25. THEODORE, C. Helicopter Flight Dynamics Simulation with Refined Aerodynamic Modeling, PhD thesis, 2000, University of Maryland, College Park.
26. GOULOS, I., PACHIDIS, V. and PILIDIS, P. Lagrangian formulation for the rapid estimation of helicopter rotor blade vibration characteristics, *Aeronaut J*, August 2014, **118**, (1206).
27. GOULOS, I. Simulation Framework Development for the Multidisciplinary Optimization of Rotorcraft, PhD thesis, 2012, School of Engineering, Cranfield University, Bedfordshire, UK.
28. GOULOS, I., PACHIDIS, V. and PILIDIS, P. Helicopter rotor blade flexibility simulation for aeroelasticity and flight dynamics applications, *J American Helicopter Soc*, October 2014, **59**, (4).
29. GOULOS, I., PACHIDIS, V. and PILIDIS, P. Flexible rotor blade dynamics for helicopter aeromechanics including comparisons with experimental data, *Aeronaut J*, March 2015, **119**, (1213).
30. GOULOS, I. and PACHIDIS, V. Real-time aeroelasticity simulation of open rotor with slender blades for the multidisciplinary design of rotorcraft, *ASME J. Eng Gas Turbines and Power*, January 2015, **137**, (1).
31. BHAGWAT, M.J. and LEISHMAN, J.G. Stability, consistency and convergence of time-marching free-vortex rotor wake algorithms, *J American Helicopter Soc*, January 2001, **46**, (1), pp 59-71.
32. GOULOS, I., GIANNAKAKIS, P., PACHIDIS, V. and PILIDIS, P. Mission performance simulation of integrated helicopter-engine systems using an aeroelastic rotor model, *ASME J Eng Gas Turbines and Power*, 2013, **135**, (9).
33. KATZ, J. and PLOTKIN, A. *Low-Speed Aerodynamics*, 2001, Cambridge Aerospace Series, Cambridge University Press, Cambridge, UK.
34. HESS, J.L. and SMITH, A.M.O. Calculation of non-lifting potential flow about arbitrary three-dimensional bodies, 1962, Douglas Aircraft Division, Report No ES 40622, Long Beach, CA, USA.
35. PETERS, D.A., BOYD, D.D. and HE, C.J. Finite-state induced-flow model for rotors in hover and forward flight *J American Helicopter Soc*, October 1989, **34**, (4), pp 5-17.
36. PETERS, D.A. and HE, C.J. Correlation of measured induced velocities with a finite-state wake model, *J American Helicopter Soc*, July 1991, **36**, (3), pp 59-70.
37. PETERS, D. How dynamic inflow survives in the competitive world of rotorcraft aerodynamics, *J American Helicopter Soc*, January 2009, **54**, (1), pp 1-15.
38. YU, K. and PETERS, D. Nonlinear state-space modeling of dynamic ground effect, *J American Helicopter Soc*, July 2005, **50**, (3), pp 259-268.
39. PETERS, D.A., MORILLO, J.A. and NELSON, A.M. New developments in dynamic wake modeling for dynamics applications, *J American Helicopter Soc*, April 2003, **48**, (2), pp 120-127.
40. ROSEN, A. and ISSER, A. A Model of the unsteady aerodynamics of a hovering helicopter rotor that includes variations of the wake geometry, *J American Helicopter Soc*, July 1995, **40**, (3), pp 6-16.
41. KROTHAPALLI, K.R. Helicopter Rotor Dynamic Inflow Modeling for Maneuvering Flight, 1998, PhD

thesis, School of Aerospace Engineering, Georgia Institute of Technology, Atlanta, GA, USA.
42. KROTHAPALLI, K.R., PRASAD, J.V.R. and PETERS, D.A. Helicopter rotor dynamic inflow modeling for maneuvering flight, *J American Helicopter Soc*, April 2001, **46**, (2), pp 129-139.
43. ZHAO, J. Dynamic Wake Distortion Model for Helicopter Maneuvering Flight, March 2005, PhD thesis, School of Aerospace Engineering, Georgia Institute of Technology, Atlanta, GA, USA.
44. PRASAD, J.V.R., FANCIULLO, T. and PETERS, J.Z.A. Toward a high fidelity inflow model for maneuvering and in-ground effect flight simulation, 9-11 May 2001, 57th Annual Forum of the American Helicopter Society, Washington, DC, USA.
45. PRASAD, J.V.R., ZHAO, J. and PETERS, D.A. Modeling of rotor dynamic wake distortion during maneuvering flight, 6-9 August 2001, 2001 AIAA Atmosphere Flight Mechanics Conference, Montreal, Canada.
46. ZHAO, J., PRASAD, J. and PETERS, D.A. Validation of a rotor dynamic wake distortion model for helicopter maneuvering flight simulation, June 2004, 60th Annual Forum of the American Helicopter Society, Baltimore, MA, USA.
47. ZHAO, J., PRASAD, J.V.R. and PETERS, D.A. Rotor dynamic wake distortion model for helicopter maneuvering flight, *J American Helicopter Soc*, October 2004, **49**, (4), pp 414-424.
48. LEISHMAN, J.G. and BEDDOES, T.S. A semi-empirical model for dynamic stall, *J American Helicopter Soc*, July 1989, **34**, (3), pp 3-17.
49. NOONAN, K.W. and BINGHAM, G.J. Two-dimensional aerodynamic characteristics of several rotorcraft aerofoils at Mach numbers from 0·35 to 0·90, January 1977, NASA Langley Research Center, TM X-73990.
50. PETERS, D.A. and HAQUANG, N. Dynamic inflow for practical applications, *J American Helicopter Soc*, October 1988, **33**, (4), pp 64-68.
51. PITT., D.M. and PETERS, D.A. Theoretical prediction of dynamicinflow derivatives, *Vertica*, March 1981, **5**, (1), pp 21-34.
52. GAONKAR, G.H. and PETERS, D.A. Effectiveness of current dynamic-inflow models in hover and forward flight, *J American Helicopter Soc*, April 1986, **31**, (2), pp 47-57.
53. STALEY, J.A. Validation of rotorcraft flight simulation program through correlation with flight data for soft-in-plane hingeless rotor, 1976, USA AMRDL-TR-75-50.
54. PETERSON, R. L., MAIER, T., LANGER, H.J. and TRANAPP, N. Correlation of wind tunnel and flight test results of a full-scale hingeless rotor, January 1994, American Helicopter Society Aeromechanics Specialist Conference, San Francisco, CA, USA.
55. PADFIELD, G.D., BASSET, P.M., DEQUIN, A.M., VON GRUNHAGEN, W., HADDON, D., HAVERDINGS, H., KAMPA, K. and MCCALLUM, A.T. Predicting rotorcraft flying qualities through simulation modelling, September 1996, A review of key results from Garteur AG06, 22nd European Rotorcraft Forum, Brighton, UK.
56. AGARD, Rotorcraft system identification, 1991, Advisory Group for Aerospace Research and Development, AGARD LS 178.
57. KALETKA, J. and GIMONET, B. Identification of extended models from BO-105 flight test data for hover flight condition, August 1995, 21st European Rotorcraft Forum, Saint Petersburg, Russia.
58. AMER, K.B. Theory of helicopter damping in pitch or roll and a comparison with flight measurements, 1950, NACA, TN 2136.
59. BRAMWELL, A.R.S., DONE, G. and BALMFORD, D. *Bramwell's Helicopter Dynamics*, 2001, Butterworth-Heinemann, Oxford, UK.
60. BAGAI, A. and LEISHMAN, J.G. Rotor free-wake modeling using a pseudo-implicit technique – including comparisons with experimental data, *J American Helicopter Soc*, April 1995, **40**, (3), pp 29-41.

APPENDIX A

Time-domain modelling of aeroelastic rotor blades for real-time flight dynamics applications

In order to capture the true aeroelastic behaviour of the main rotor, it is necessary that the time-dependent aerodynamic and inertial loads exerted on the blades are accurately predicted. The helicopter may be pitching, rolling, climbing, or turning. The inertial velocity and acceleration terms associated with the motion of the helicopter as well as the deformation of the elastic blades, need to be accounted for. Therefore, an effective treatment of the blade's nonlinear kinematics is required. This appendix presents the mathematical derivation of a comprehensive mathematical model for the treatment of elastic blade dynamics in helicopter aeromechanics applications.

6.0.1 Three-dimensional kinematics of elastic blades

Figures 19(a), (b), and (c) demonstrate the standard flight dynamics reference frames, namely; fuselage axes system, rotor hub axes, and hub-wind axes system, respectively. The origin of the fuselage axes frame is located at the helicopter's centre of gravity (CG). The corresponding unit vectors $\mathbf{e}_x^{fus}, \mathbf{e}_y^{fus}, \mathbf{e}_z^{fus}$ essentially point forward, starboard, and downward in that order as shown in Fig. 19(a). The rotor hub axes system is aligned with the shaft and has its origin located at the centre of the rotor hub. The respective unit vectors $\mathbf{e}_x^{h}$, $\mathbf{e}_y^{h}$, $\mathbf{e}_z^{h}$ are obtained by rotating the vectors of the fuselage system as depicted in Fig. 19(b) so as to factor in the longitudinal shaft tilt angle γ_s. The origin of the hub-wind axes system is identical to that of the hub frame. The hub-wind unit vectors $\mathbf{e}_x^{hw}$, $\mathbf{e}_y^{hw}$, $\mathbf{e}_x^{hw}$ are acquired by rotating the hub system as shown in Fig. 19(c) in order to account for the rotor side-slip angle $\psi_w = \text{Arcsin}\dfrac{v_h}{\sqrt{u_h^2 + v_h^2}}$. This process aligns the system unit vector $\mathbf{e}_x^{hw}$, with the resultant edge-wise rotor hub velocity component $\sqrt{u_h^2 + v_h^2}$.

The linear and angular velocity components of the helicopter fuselage, depicted in Fig. 19(a), are classified in vector notation in the fuselage axes system as follows; $\mathbf{u} = [u\ v\ w]^T$, $\boldsymbol{\omega} = [p\ q\ r]^T$. Identical expressions are used for the corresponding acceleration vectors $\dot{\mathbf{u}}$ and $\dot{\boldsymbol{\omega}}$. A global non-rotating reference frame O is defined which is aligned with the main rotor shaft. The O frame's origin is also located at the centre of the main rotor hub. Figure 19(c) shows that the O system's unit vectors are related to the hub-wind axes vectors as follows; $\mathbf{e}_x^{o} = -\mathbf{e}_x^{hw}$, $\mathbf{e}_y^{o} = \mathbf{e}_y^{hw}$, $\mathbf{e}_z^{o} = -\mathbf{e}_z^{hw}$. The respective linear and angular velocity components, $\mathbf{u}_o = [u_0\ v_0\ w_0]^T$ and $\boldsymbol{\omega}_o = [p_0\ q_0\ r_0]^T$, which result from the corresponding fuselage motions, are expressed in the global non-rotating O reference frame as follows:

$$\mathbf{u}_o = \Gamma \begin{Bmatrix} u - q \cdot h_r \\ v + p \cdot h_r - r \cdot x_{cg} \\ w + q \cdot x_{cg} \end{Bmatrix} \quad \ldots (54)$$

$$\dot{\omega}_o = \Gamma \begin{Bmatrix} p \\ q \\ r \end{Bmatrix} \quad \ldots (55)$$

where $\boldsymbol{\Gamma}$ expresses vector transformation from the fuselage axes system to the global non-rotating O frame. This transformation is shown graphically in Fig. 19 and is defined mathematically as:

https://doi.org/10.1017/S0001924000010563 Published online by Cambridge University Press

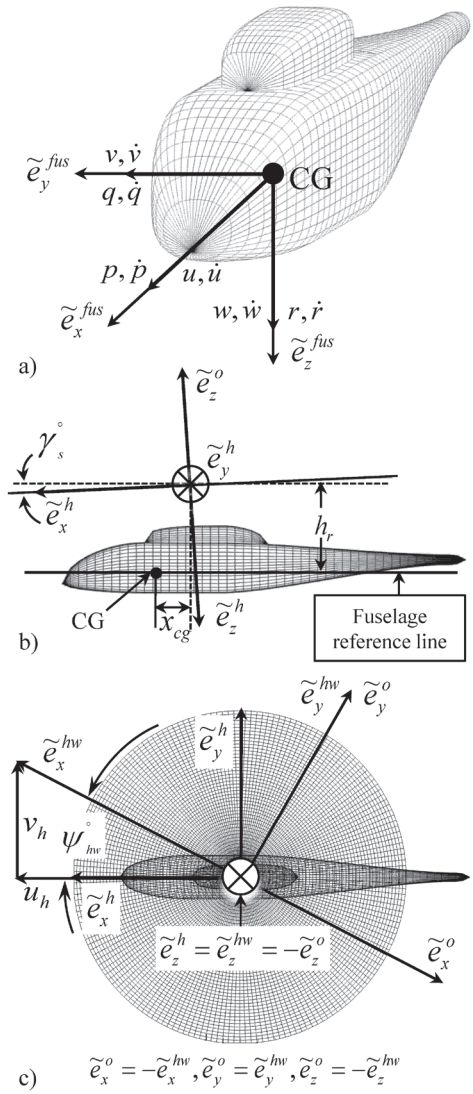

Figure 19. Standard non-rotating reference frames for helicopter flight dynamics: (a) Fuselage axes system, (b) Main rotor hub axes system, (c) Main rotor hub-wind axes system.

$$\mathbf{\Gamma} = \begin{bmatrix} -1 & 0 & 0 \\ 0 & 1 & 0 \\ 0 & 0 & -1 \end{bmatrix} \begin{bmatrix} \mathrm{Cos}(\psi_w) & \mathrm{Sin}(\psi_w) & 0 \\ -\mathrm{Sin}(\psi_w) & \mathrm{Cos}(\psi_w) & 0 \\ 0 & 0 & 1 \end{bmatrix} \begin{bmatrix} \mathrm{Cos}(\gamma_s) & 0 & \mathrm{Sin}(\gamma_s) \\ 0 & 1 & 0 \\ -\mathrm{Sin}(\gamma_s) & 0 & \mathrm{Cos}(\gamma_s) \end{bmatrix} \quad \ldots (56)$$

It is noted that h_r is the orthogonal distance between the rotor hub and the fuselage reference line, positive upwards as shown in Fig. 19(b). x_{cg} signifies the orthogonal distance between the

https://doi.org/10.1017/S0001924000010563 Published online by Cambridge University Press

helicopter's CG and the point on the fuselage reference line located directly below the rotor hub, positive for a forward CG location (Fig. 19(b). Expressions identical to those given by Equations (54) and (55) are used for the corresponding linear and angular acceleration components; $\dot{\mathbf{u}}_{\mathbf{o}} = [\dot{u}_0\ \dot{v}_0\ \dot{w}_0]^T$ and $\dot{\boldsymbol{\omega}}_{\mathbf{o}} = [\dot{p}_0\ \dot{q}_0\ \dot{r}_0]^T$, respectively.

A separate set of rotating reference systems is utilised as illustrated in Fig. 20. The mathematical model described in this paper places each beam element $p(r,t)$ of local radius r at time t, on the rotor blade's mean elastic axis. Each $p(r,t)$ element is treated as a material object with differential mass $dm = \rho A(r)dr$. The centre gravity of $p(r,t)$ is assumed to be located on the blade chord and offset from the elastic axis by a user-defined amount $Y_{offset}(r)$. A rotating reference system A_i, $i = 1, \ldots N_b$ is specified for each of the N_b rotor blades as shown in Fig. 20(a). The rotating A_i frame is aligned with the time-dependent positioning of the ith blade root/hinge. The position vector of the origin of A_i is expressed in the global non-rotating O frame of reference as: $\mathbf{r}_{A_i/O} = [eR\text{Cos}\,\psi_i(t)\ eR\text{Sin}\,\psi_i(t)\ 0]^T$, where $\psi_i(t)$ is the azimuth angle of the ith blade and e is the blade root/hinge offset distance from the centre of rotation as a fraction of blade radius R.

For a rotor with predefined values of pre-cone, pre-sweep, and collective pitch angles, a tensor operator $\mathbf{A}_i$ can be specified as the following non-permutable sequence of rotations:

$$\mathbf{A}_i = \boldsymbol{\Theta}_0 \mathbf{B}_{pre} \mathbf{Z}_{pre} \boldsymbol{\Psi}_i \qquad \ldots (57)$$

Application of $\mathbf{A}_i$ to any vector expressed in the global non-rotating O frame yields the corresponding expression of the same vector in the rotating system A_i. The matrices $\boldsymbol{\Theta}_0$, $\mathbf{B}_{pre}$, $\mathbf{Z}_{pre}$ and $\boldsymbol{\Psi}_i$ describe rotations about the corresponding angles and have been provided in Refs 27 and 28. It can be observed that only collective pitch Θ_0 is applied for the derivation of $\mathbf{A}_i$. The effects of cyclic pitch, blade twist, and torsion will be accounted for individually in the rotating A_i system.

The absolute angular velocity and acceleration vectors of the origin of A_i can be expressed as: $\dot{\boldsymbol{\omega}}_0 = [p_0\ q_0\ (r_0 + \Omega)]^T$ and $\dot{\boldsymbol{\omega}}_{A_i} = [\dot{p}_0\ \dot{r}_0\ (\dot{q}_0\ \dot{r}_0 + \dot{\Omega}]^T$, in that order. The corresponding absolute linear velocity and acceleration vectors are given by:

$$\mathbf{u}_{A_i} = \mathbf{u}_o + \boldsymbol{\omega}_{A_i} \times \mathbf{r}_{A_i/O} \qquad \ldots (58)$$

$$\mathbf{a}_{A_i} = \dot{\mathbf{u}}_o + \boldsymbol{\omega}_{A_i} \times (\boldsymbol{\omega}_{A_i} \times \mathbf{r}_{A_i}) + \dot{\boldsymbol{\omega}}_{A_i} \times \mathbf{r}_{A_i/O} \qquad \ldots (59)$$

The position vector of beam element $p(r,t)$ relative to the origin of and expressed in the rotating A_i frame (Fig. 20(b)) is given by:

$$\mathbf{r}_{p/A_i}^{A_i} = \begin{Bmatrix} (r - eR)\,\text{Cos}\,\beta(r,t)\,\text{Cos}\,\zeta(r,t) \\ -(r - eR)\,\text{Sin}\,\zeta(r,t) \\ (r - eR)\,\text{Sin}\,\beta(r,t) \end{Bmatrix} \qquad \ldots (60)$$

where $\beta(r,t)$ and $\zeta(r,t)$ are the equivalent flap and lag angles respectively. These are defined in A_i (Fig. 20(b)) as follows:

$$\beta(r,t)/\zeta(r,t) = \text{Arcsin}\,\frac{w^{F/L}(r,t)}{r - eR} \qquad \ldots (61)$$

where $w^{F/L}(r,t)$ denotes the time-dependent flap/lag transverse displacement of the blade. The first and second derivatives of Equation (61) lead to the relative angular velocity and acceleration components of $p(r,t)$. These can be written in A_i as:

https://doi.org/10.1017/S0001924000010563 Published online by Cambridge University Press

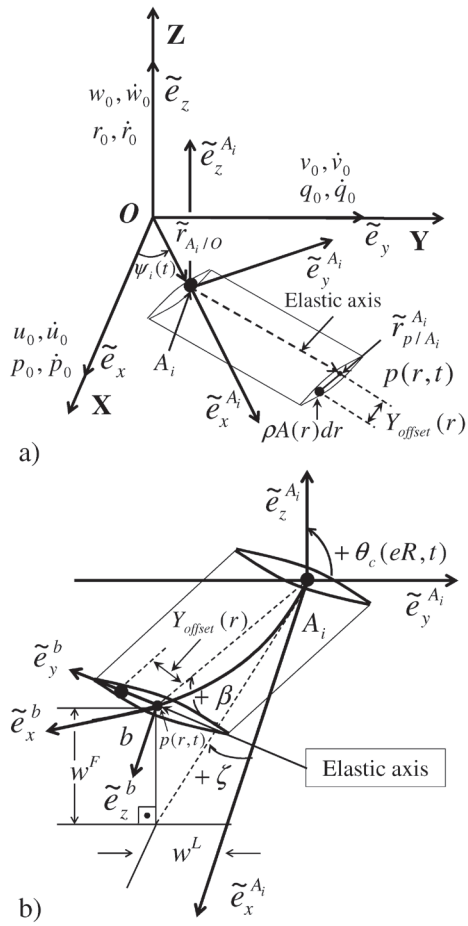

Figure 20. Reference systems used for the description of elastic blade kinematics: (a) Global non-rotating reference system *O*, (b) Rotating and blade element reference frames (A_i and *b*, respectively).

$$\dot{\beta}(r,t)/\dot{\zeta}(r,t) = \frac{\dot{w}^{F/L}(r,t)}{\sqrt{(r-eR)^2 - w^{F/L}(r,t)^2}} \quad \ldots (62)$$

$$\ddot{\beta}(r,t)/\ddot{\zeta}(r,t) = \frac{\ddot{w}^{F/L}(r,t)}{\sqrt{(r-eR)^2 - w^{F/L}(r,t)^2}} + \frac{w^{F/L}(r,t)\cdot\dot{w}^{F/L}(r,t)^2}{((r-eR)^2 - w^{F/L}(r,t)^2)^{3/2}} \quad \ldots (63)$$

Considering hingeless rotor blade configurations where cyclic pitch is applied inboard of the root/hinge location, the relative angular velocity and acceleration vectors of $p(r,t)$ can be expressed in the rotating A_i reference system as follows:

https://doi.org/10.1017/S0001924000010563 Published online by Cambridge University Press

$$\omega^{A_i}_{p/A_i}/\dot{\omega}^{A_i}_{p/A_i} = \begin{Bmatrix} \dot{\theta}_c(eR,t) \\ -\dot{\beta}(r,t) \\ -\dot{\zeta}(r,t) \end{Bmatrix} / \begin{Bmatrix} \ddot{\theta}_c(eR,t) \\ -\ddot{\beta}(r,t) \\ -\ddot{\zeta}(r,t) \end{Bmatrix} \quad \ldots (64)$$

where $\theta_c(eR,t)$ is the applied cyclic pitch at the rotor hub. Reference 29 has provided the corresponding expressions for $\dot{\boldsymbol{\omega}}^{A_i}_{p/A_i}/\dot{\boldsymbol{\omega}}^{A_i}_{p/A_i}$ considering articulated rotor blades that incorporate cyclic pitch application outboard of the root/hinge location.

The linear velocity and acceleration vectors of $p(r,t)$ relative to the origin of and expressed in the A_i frame are given by:

$$\mathbf{u}^{A_i}_{p/A_i} = \boldsymbol{\omega}^{A_i}_{p/A_i} \times \mathbf{r}^{A_i}_{p/A_i} \quad \ldots (65)$$

$$\mathbf{a}^{A_i}_{p/A_i} = \boldsymbol{\omega}^{A_i}_{p/A_i} \times (\boldsymbol{\omega}^{A_i}_{p/A_i} \times \mathbf{r}^{A_i}_{p/A_i}) + \dot{\boldsymbol{\omega}}^{A_i}_{p/A_i} \times \mathbf{r}^{A_i}_{p/A_i} \quad \ldots (66)$$

which along with the vector $\mathbf{r}^{Ai}_{p/A_i}$, they can be transformed to the global O system as follows:

$$\mathbf{r}^{O}_{p/A_i} = \mathbf{A}_i^{-1}\mathbf{u}^{A_i}_{p/A_i} \quad \ldots (67)$$

$$\mathbf{u}^{O}_{p/A_i} = \mathbf{A}_i^{-1}\mathbf{u}^{A_i}_{p/A_i} \quad \ldots (68)$$

$$\mathbf{a}^{O}_{p/A_i} = \mathbf{A}_i^{-1}\mathbf{a}^{A_i}_{p/A_i} \quad \ldots (69)$$

The absolute velocity and acceleration vectors of $p(r,t)$ can now be expressed in the O frame:

$$\mathbf{u}^{O}_{p} = \mathbf{u}_{A_i} + \mathbf{u}^{O}_{p/A_i} + \boldsymbol{\omega}_{A_i} \times \mathbf{r}^{O}_{p/A_i} \quad \ldots (70)$$

$$\mathbf{a}^{O}_{p} = \mathbf{a}_{A_i} + \mathbf{a}^{O}_{p/A_i} + 2 \cdot \boldsymbol{\omega}_{A_i} \times \mathbf{u}^{O}_{p/A_i} + \dot{\boldsymbol{\omega}}_{A_i} \times \mathbf{r}^{O}_{p/A_i} + \boldsymbol{\omega}_{A_i} \times (\boldsymbol{\omega}_{A_i} \times \mathbf{r}^{O}_{p/A_i}) \quad \ldots (71)$$

It is of relevance to express the obtained velocity and acceleration vectors in a blade element fixed reference frame b. This not only provides the inertial local flow-field conditions which is essential input for any aerodynamic theory, but it also enables for D'Alembert's principle of superposition to be utilised with respect to the aerodynamic and inertial loads. Figure 20(b) illustrates the local blade element system of $p(r,t)$. The system orientation is specified by unit vectors $\mathbf{e}^b_x$, $\mathbf{e}^b_y$, and $\mathbf{e}^b_z$.

The global velocity and acceleration vectors expressed by Equations (70) and(71) can be converted to the local blade element fixed co-ordinate system b using the following transformation:

$$\mathbf{u}^{b}_{p} = \mathbf{T}^{b}_{i}\mathbf{u}^{O}_{p} \quad \ldots (72)$$

$$\mathbf{a}^{b}_{p} = \mathbf{T}^{b}_{i}\mathbf{a}^{O}_{p} \quad \ldots (73)$$

where $\mathbf{T}^b_i$ is a tensor operator that relates any vector expressed in the global O frame directly to

https://doi.org/10.1017/S0001924000010563 Published online by Cambridge University Press

the local blade element co-ordinate system , It is defined as the following sequence of rotations:

$$\mathbf{T}_i^b = \boldsymbol{\theta}_c \boldsymbol{\beta} \boldsymbol{\zeta} \boldsymbol{\theta}_T \boldsymbol{\theta}_{tw} \boldsymbol{\lambda} \mathbf{A}_i \quad \ldots (74)$$

where $\boldsymbol{\lambda}$, $\boldsymbol{\theta}_{tw}$, $\boldsymbol{\theta}_T$, $\boldsymbol{\zeta}$, $\boldsymbol{\beta}$, and $\boldsymbol{\theta}_c$ are rotation matrices for blade element sweep, pre-twist, torsion, lag, flap, and cyclic pitch respectively. These matrices have been provided in Refs 27 and 28.

6.0.2 Finite-difference treatment of elastic blade motion

Evaluation of Equations (62) and (63) requires determination of the first and second temporal derivatives of flap/lag transverse displacement $w^{F/L}(r,t)$. Within this work, the time-derivatives of interest are evaluated numerically using a modified version of the second-order backward-difference scheme, originally developed in Ref. 31 for time-accurate free-wake analysis. Reference 31 has analysed the scheme's stability characteristics where it has been shown that it is stable with positive damping.

The numerical differentiation algorithm of Ref. 31 approximates the first temporal derivative of displacement at time = $t + \Delta t/2$, Δt being the employed time-marching step. Application of the original scheme on the first temporal derivatives of $w^{F/L}$ taken at $t + \Delta t/2$, $t - \Delta t/2$, $t - 3\Delta t/2$, etc., essentially provides the second temporal derivative of displacement at time = t. However, the present model requires estimates of both first and second temporal derivatives of displacement at the same time instant. The original scheme is therefore modified by assuming

$$w^{F/L}(r,t+\Delta t/2) \approx \frac{w^{F/L}(r,t) + w^{F/L}(r,t+\Delta t)}{2}$$

in order to provide both derivatives at time = t. The modified algorithms give:

$$\frac{\partial w^{F/L}(r,t)}{\partial t} \approx \frac{3w^{F/L}(r,t+\Delta t) + 2w^{F/L}(r,t) - 4w^{F/L}(r,t-\Delta t)}{8\Delta t} + \frac{-2w^{F/L}(r,t-2\Delta t) + w^{F/L}(r,t-3\Delta t)}{8\Delta t} \quad \ldots (75)$$

$$\frac{\partial^2 w^{F/L}(r,t)}{\partial t^2} \approx \frac{3\dot{w}^{F/L}(r,t+\Delta t/2) - \dot{w}^{F/L}(r,t-\Delta t/2)}{4\Delta t} + \frac{-3\dot{w}^{F/L}(r,t-3\Delta t/2) + \dot{w}^{F/L}(r,t-5\Delta t/2)}{4\Delta t} \quad \ldots (76)$$

It is noted that the modified finite-difference schemes expressed by Equations (75) and (76) are also applied for the approximation of the first and second temporal derivatives of $\theta^T(r,t)$, respectively.

It is emphasised that initial versions of the model that incorporated typical second-order central finite-differences, exhibited significant instabilities and thus required very small time-steps for stable simulation. This essentially prohibited applicability in real-time. However, the employed schemes expressed by Equations (75) and (76) essentially alleviated the aforementioned issues and stable simulations can be performed with time-steps leading to equivalent azimuth-steps of the order of 20°. Thus, utilisation of the particular algorithms not only results in increased simulation stability, but also in significant reduction of computational time. This essentially constitutes an enabling technology for application of the proposed flight dynamics simulation model in real-time.

https://doi.org/10.1017/S0001924000010563 Published online by Cambridge University Press

6.0.3 Numerical integration of nonlinear aeroelastic blade loads

Using D'Alembert's principle of superposition for the aerodynamic and inertial force/moment loads expressed in the rotating blade element co-ordinate system b, and subsequent conversion to the global non-rotating O frame, yields the following differential expressions:

$$d\mathbf{f}_p^O = [\mathbf{T}_i^b]^{-1}\{\mathbf{f}_{aero}^b - \rho A(r)\mathbf{a}_p^b\}dr \quad \ldots(77)$$

$$d\mathbf{m}_p^O = [\mathbf{T}_i^b]^{-1}\{\mathbf{m}_{aero}^b - \rho I_p(r)\ddot{\boldsymbol{\theta}}^T - \rho A(r)\{\mathbf{r}_p^{b,offset} \times \mathbf{a}_p^b\}\}dr \quad \ldots(78)$$

where $\ddot{\boldsymbol{\theta}}^T = [\ddot{\theta}^T(r,t)\ 0\ 0\ ]^T$. The vector $\mathbf{r}_p^{b,offset} = [0\ Y_{offset}(r)\ 0]^T$ denotes the aerofoil centre gravity offset from the blade's elastic axis. The vectors $\mathbf{f}_{aero}^b$, $\mathbf{m}_{aero}^b$ signify the aerodynamic forces and moments per unit length respectively. These can be obtained using any aerodynamic theory.

The total rotor forces and moments ($\mathbf{F}_{rotor}^O(t)$ and $\mathbf{T}_{rotor}^O(t)$) can be estimated by summing the contributions of the individual blades; $\mathbf{F}_{rotor}^O(t) = \sum_{i=1}^{N_b}\mathbf{F}_i^O(t)$, $\mathbf{T}_{rotor}^O(t) = \sum_{i=1}^{N_b}\mathbf{T}_i^O(t)$, where $\mathbf{F}_i^O(t) = \int_{eR}^{R} d\mathbf{f}_p^O$, $i = 1 \ldots N_b$. The total moment that a rotor blade exercises about the origin of the global O frame is given by; $\mathbf{T}_i^O(t) = \mathbf{T}_{i,offset}^O(t) + \mathbf{T}_{i,root}^O(t)$, $i = 1 \ldots N_b$. The component $\mathbf{T}_{i,offset}^O(t)$ is the moment that the blade applies about the origin due to its hinge offset from the centre of rotation and is given by $\mathbf{T}_{i,offset}^O(t) = \mathbf{r}_{A_i/O} \times \mathbf{F}_i^O(t)$.

The component $\mathbf{T}_{i,root}^O(t)$ is the moment that the blade exerts directly on its root/hinge due to the root/hinge spring stiffness. For a hingeless rotor blade, the component $\mathbf{T}_{i,root}^O(t)$ is due to the effective stiffness of the blade root and can be expressed as:

$$\mathbf{T}_{i,root}^O(t) = \mathbf{A}_i^{-1}\begin{Bmatrix} GJ(eR)\theta'^T(eR,t) \\ -EI^F(eR)w''^F(eR,t) \\ -EI^L(eR)w''^L(eR,t) \end{Bmatrix}, \quad i = 1,\ldots N_b \quad \ldots(79)$$

Alternatively, $\mathbf{T}_{i,root}^O(t)$ can be obtained by integrating all aerodynamic and inertial loads acting on the blade at the respective time-instant t. This process yields:

$$\mathbf{T}_{i,root}^O(t) = \int_{eR}^{R}\mathbf{r}_{p/A_i}^O \times \mathrm{d}\mathbf{f}_p^O + \int_{eR}^{R}\mathrm{d}\mathbf{m}_p^O, \quad i = 1,\ldots N_b \quad \ldots(80)$$

For a spring-hinged articulated blade, $\mathbf{T}_{i,root}^O(t)$ is determined by the local flap/lag angles and the employed spring stiffness constants.

The overall rotor force and moment vectors about the helicopter's CG (Fig. 19(a)) can now be computed directly in the fuselage axes system using the following expressions:

$$\mathbf{F}_{rotor}^{fus}(t) = \boldsymbol{\Gamma}^{-1}\mathbf{F}_{rotor}^O(t) \quad \ldots(81)$$

$$\mathbf{T}_{rotor}^{fus}(t) = \boldsymbol{\Gamma}^{-1}\mathbf{T}_{rotor}^O(t) + [-x_{cg} \quad 0 \quad -h_r]^T \times \{\boldsymbol{\Gamma}^{-1}\mathbf{F}_{rotor}^O(t)\} \quad \ldots(82)$$

Equations (81) and (82) can be used without any modification by any simulation code that utilises the fuselage axes reference system as illustrated in Fig. 19(a), for the calculation of the time-dependent three-dimensional rotor force and moment loads exerted on the aircraft.

https://doi.org/10.1017/S0001924000010563 Published online by Cambridge University Press